Ab initio study of magnetic effects at material interfaces

by

Dicle Yeşilleten

Submitted to the Department of Physics
in partial fulfillment of the requirements for the degree of

Doctor of Philosophy in Physics

at the

MASSACHUSETTS INSTITUTE OF TECHNOLOGY
[February 2003]
January 2003

Author .....
Department of Physics
December 19, 2002

Certified by .....
Tomás Alberto Arias
Associate Professor, Cornell
Thesis Supervisor

Certified by .....
John D. Joannopoulos
Professor, MIT
Thesis Supervisor

Accepted by .....
Chairman, Department Committee on Graduate Students

Ab initio study of magnetic effects at material interfaces

by

Dicle Yeşilleten

Submitted to the Department of Physics
on December 28, 2002, in partial fulfillment of the
requirements for the degree of
Doctor of Philosophy in Physics

Abstract

Fairly little is known from a fundamental first principles level about the role of magnetism at material interfaces. This thesis will address (a) changes in spin density at grain boundaries and surfaces; (b) the impact of these changes on interfacial energies and structures; and (c) the behavior of point defects (including vacancies, impurities and adatoms) at interfaces.

We first develop a simple, general energy functional for ferromagnetic materials based upon a local spin density extension to the Stoner theory of itinerant ferromagnetism and use it to explore the physics of grain boundaries in iron, such as interfacial energies, structures, and magnetic effects. Our results show that magnetism, in addition to driving structural relaxation, also greatly enhances intergranular cohesion in iron.

To explore the effects of point defects at material interfaces, we present an extensive study of non-magnetic Molybdenum grain boundaries. This trend study which is carried out with an appropriate atomistic potential reveals an important set of structural phase transitions involving the exchange of vacancies with the surrounding bulk material. We also show that the same mechanism of vacancy driven structural phase transitions appear when these systems are studied with first principles techniques.

Finally, we explore the role of magnetism in the diffusion of adatoms and vacancy migration at surfaces and steps in a transition path study of Cobalt.

Thesis Supervisor: Tomás Alberto Arias
Title: Associate Professor, Cornell

Thesis Supervisor: John D. Joannopoulos
Title: Professor, MIT

Acknowledgments

I would like to thank my family for their unconditional love and support. Nothing would have been possible without them.

I would also like to thank my advisor Prof Tomas Arias for all his help, support, patience and understanding through the eight years we have worked together.

I would like to thank Nancy Savioli, Patricia Solakoff, Alicia Duarte and Brian Canavan from the Physics Education Office and Margaret O'Meara from Condensed Matter Theory Department for their sincere friendship through the years. Without them, getting through years of heartache would have been impossible.

I would also like to thank my fellow graduate student friends Sohrab Ismail-Beigi, Gabor Csyani, Daren Segall, Torkel Engeness, Hande Ustunel, and Ivan Daykov for all their help, patience and understanding.

Peter Murphy and Ian Astbury cannot go unacknowledged for their musical contributions. I thank them with all my heart.

Finally, I thank Baran for everything that matters.

"Everything in the world is happening all together at once and we, with our myopic little minds, are working it out step by step... One track minds in an infinitely tracked universe." -Alan Watts

Contents

List of Figures

List of Tables

Chapter 1

Introduction

Ever since the dawn of humankind, man has tried to understand the nature around him, not only to bring some meaning to his existance, but also to use this understanding and the tools developed through this understanding to aid in his survival. Ancient men, without being aware of the underlying principles, have stared at the stars and invented fictituous gods to protect over them, used mechanical tools, for example levers, wheels, pulleys and later, lenses to overcome their weaknesses, like lack of strong body weapons such as sharp teeth and claws, and lack of better vision and better sense of smell, endowed upon him by evolution.

Even though man has used these mechanical tools as he was trying to evolve, history shows that scientific methods for astronomy, mathematics, chemistry and medicine have already been vigorously developed as early as circa 3000 BC during the time of the Old Kingdom in Egypt. However, our modern understanding of science has emerged as late as the sixteenth century with Johannes Keppler's (1571-1630) study of planetory motion, experimental studies of electromagnetism by Otto von Guericke (1602-1686), Pieter van Musschenbroek (1692-1761), Benjamin Franklin (1706-1790), Joseph Priestley (1733-1804), and Sir Isaac Newton's (1642-1727) formulation of laws of mechanics, as well as Charles-Augustin de Coulomb (1736-1806), Michael Faraday (1791-1867) and James Clerk Maxwell's (1831-1879) formulation of electromagnetism. Although mechanics and electromagnetism proved to be accurate in their own realm of physics, development of quantum mechanics in the twentieth century by Max Planck

(1858-1947), Albert Einstein (1879-1955), Niels Bohr (1885-1962), Arthur Compton (1892-1962), Louis de Broglie (1892-1987), Werner Heisenberg (1901-1976), Wolfgang Pauli (1900-1958), Paul Dirac (1902-1984), and Erwin Schrödinger (1887-1961) has opened new doors of understanding and appreciation of the world we live in.

Today we see nature as layers of intertwined phenomena, each of which we try to understand using various different theories and methods developed over the years. As the astrophysicist is studying the effects of sun's magnetic field on earth, the condensed matter physicist aims to understand materials and their properties, both through experimental studies and through the theoretical framework developed and perfected over the years. The work presented in this thesis aims to shed some light on the properties of industrially important materials, in particular ferromagnetic iron, brittle molybdenum and magnetic cobalt, by studying defects, so as to explain the intruiging nature of interfaces in materials.

According to solid state physics, most materials in their solid form consist of crystals, with perfectly periodic environments. However, as nothing is perfect and flawless in nature, impurities and faults at crystal structure dominate materials properties. In this thesis, we concentrate on these flaws, in particular grain boundaries (where two or more perfect bulk-like grains or islands are attached to each other at different orientations and twist and tilt angles), surfaces (where the bulk periodicity is broken and material is exposed to vacuum) and vacancies (where only a single atom is missing in the perfect bulk environment) to explore real-life like systems.

Condensed matter theorist is equipped with different techniques to study such systems, such as atomistic studies, density functional theory and intermediate tight-binding approaches, all of which have their own advantages as well as weaknesses. All of these methods have been discussed in detail and employed in this work.

In Chapter 2, in order to understand the effects of magnetism in iron, we refrain from atomistic models, which coarse-grain over the electronic degrees of freedom completely, giving a very simple yet unrealistic description of iron as they ignore magnetism. Instead, we develop a simple, tight-binding description of iron, using a general energy functional based upon a local spin density extension to the Stoner the-

ory of itinerant ferromagnetism. We perform a trend study of the grain boundaries in iron and show that magnetism drives structural relaxation, and also greatly enhances intergranular cohesion in iron.

In Chapter 3, we shift our focus from magnetism to the effects of point defects at material interfaces, and employ an appropriate atomistic model to perform an extensive study of non-magnetic Molybdenum grain boundaries. This work reveals an important set of structural phase transitions involving the exchange of vacancies with the surrounding bulk material. Equipped with this knowledge, in Chapter 4, we use density functional theory, which provides a rigorous, first principles approach to finding the ground-state energy and single-particle properties of any electronic system, to delve deeper into brittle nature of molybdenum. Our work shows that the same mechanism of vacancy driven structural phase transitions appear when these systems are studied with first principles techniques, which gives proof to the conclusions of Chapter 3.

As Chapter 2 has shown that magnetism plays a key role in structural relaxations and intergranular cohesion, Chapters 3 and 4 reveals that impurities such as vacancies also act as driving forces in structural relaxations as well as fracture. However, as all this work concentrates on grain boundaries in materials, in Chapter 5, we shift focus from bulk-like defects to surfaces in magnetic cobalt. We first study the diffusion of adatoms at surfaces with an atomistic transition path study of cobalt. We then employ density functional theory, which when combined with the local-density approximation to the exchange-correlation energy, provides an accurate and computationally feasible method for calculating the Born-Oppenheimer energy, atomic forces and spin densities for any atomic configuration. Our results demonstrate a close link between the motion of the adatom and the spin configuration of the material.

Chapter 2

A tight-binding, Stoner-exchange description of non-crystalline iron

Abstract:

We present a study of the active microscopic processes which control the physical behavior of inhomogeneous systems of iron. We find that the underlying active degrees of freedom may be taken as consisting of only the nature of bonding between the atomic d-orbitals and the spin polarization on each atom. We demonstrate this by presenting a simple coarse-grained Hamiltonian. After fitting a limited set of parameters to the primitive physical properties of bulk α-iron, we find that our Hamiltonian accurately predicts such complex phenomena as the energetics and magnetic structure of grain boundaries, the melting temperature at constant volume, and the activation energy for self-diffusion in the liquid state.

2.1 Introduction

Our current understanding of the microscopic behavior of inhomogeneous systems of iron, whether bulk material incorporating defects or the liquid state, is based on two very different types of models: full-blown *ab initio* spin-dependent total energy density-functional calculations[14] and calculations of lattice configurations based upon empirical interatomic potential models, such as the embedded atom method (EAM)[48, 28, 56, 44]. *Ab initio* calculations treat explicitly the relevant many-body physics of the electronic degrees of freedom at lower temperatures where spin fluctuations are not important. However, these calculations are very demanding computationally. In contrast, the EAM coarse-grains over the electronic degrees of freedom completely[48], giving a very simple description which allows the study of complex phenomena.

The computational demands of the density-functional calculations have so far limited the application of these extremely detailed studies in iron to bulk crystals and the simplest extended defects, such as small cluster studies for the $\Sigma 3(111)$[24, 13, 35] and $\Sigma 5(310)$[9] grain boundaries. The computational demands of this approach preclude the possibility of understanding the microscopic phenomena controlling the behavior of more complex grain boundaries, dislocations, and processes which occur over long time-scales, such as melting and self-diffusion in the liquid.

EAM treatments, on the other hand, are feasible computationally for dislocation [56] and fracture studies [44]. However, they are overly simple, and by ignoring variations in exchange effects, they neglect processes such as the exchange mechanism which control the ground-state lattice structure and the behavior of extended defects.

The works by Hasegawa and Pettifor[40] and Zhong, Overney, and Tomanek[51] present intermediate descriptions of iron which include these exchange effects explicitly. Hasegawa and Pettifor go beyond mean-field Stoner theory[49] and include many-body spin fluctuation effects[19, 18] in a d-band tight-binding description. This description reproduces well the phase diagram of iron at higher temperatures. They also show that below $T_f \approx 500$ K, their spin-fluctuation description reduces to Stoner

theory. The results of Hasegawa and Pettifor thus lend support to the use of models such as that of Zhong, Overney, and Tomanek[51] at temperatures below T_f. This latter model describes bulk crystalline iron based upon a combination of an *spd* tight-binding approximation and the Stoner theory of itinerant ferromagnetism [49].

The aforementioned works in the previous paragraph, while providing a promising description intermediate to the embedded atom method and full blown density-functional calculations, were limited to homogeneous bulk crystalline phases only. In this paper, we extend such an intermediate-level description of iron to treat inhomogeneous systems, in particular grain boundary structures and the liquid state. We shall use the Stoner description to treat the local atomic spins as active degrees of freedom, and follow Hasegawa and Pettifor and in considering only bonding among the *d*-states.

While similar in spirit to the previous tight-binding based descriptions, the coarse-grained Hamiltonian which we present differs in two important aspects. The most significant difference is that the present model incorporates a local, environmentally dependent treatment of the Stoner parameter, thereby allowing one to study inhomogeneous structures. In addition, to enable a simple Hellman-Feynman-like treatment of the forces, which is necessary for relaxing defect structures and for molecular dynamics studies, we recast the total energy functional in a direct form rather than as an integral over the densities of states for the majority and the minority carriers[51].

2.2 Tight-Binding model

2.2.1 Overview

The present Hamiltonian includes three basic contributions to the energy: (1) single-particle terms to describe bonding among electrons, (2) exchange effects to describe spin polarization effects, and (3) a repulsive potential between atomic cores. This section introduces the various terms of the Hamiltonian. Section 2.3 describes the parameterization of each of these terms.

We represent the free energy for a periodic supercell of material as

$$\begin{aligned} E(\mu_\uparrow, \mu_\downarrow) &= \sum_{nk\sigma} w_k \left(f_{nk\sigma}\epsilon_{nk} - T s_{nk\sigma}\right) \\ &+ \frac{b}{2}\sum_{\alpha\neq\beta} e^{-p\tau_{\alpha\beta}} \\ &- \frac{1}{4}\sum_{\alpha} I_\alpha \left(n_{\sigma=+1}(\alpha) - n_{\sigma=-1}(\alpha)\right)^2, \end{aligned} \tag{2.1}$$

where the Fermionic entropy is

$$s_{nk\sigma} \equiv -k_B \left[f_{nk\sigma} \ln f_{nk\sigma} + (1 - f_{nk\sigma}) \ln (1 - f_{nk\sigma})\right]. \tag{2.2}$$

Here, n labels the electronic bands and k varies over an appropriately chosen reciprocal space mesh with weights w_k for integration over the Brillouin zone. The band structure sum also extends over the spin index $\sigma = \pm 1$. The $f_{nk\sigma}$ are Fermi-Dirac occupation numbers,

$$f_{nk\sigma} = \frac{1}{e^{(\epsilon_{nk} - \mu_\sigma)/k_B T} + 1}, \tag{2.3}$$

where μ_σ is the chemical potential of spin channel σ. The separate Fermi levels for the two spin channels are adjusted separately to minimize the total energy while maintaining the correct total number of electrons. The energy levels ϵ_{nk} are obtained by diagonalizing a tight-binding Hamiltonian at each point of the Brillouin zone,

$$\sum_{\beta m_z'} H_k(\alpha m_z, \beta m_z')\psi_{nk}(\beta m_z') = \epsilon_{nk}\psi_{nk}(\alpha m_z). \tag{2.4}$$

Here, $H_k(\alpha m_z, \beta m_z')$ is the matrix element at point k in the Brillouin zone connecting the m_z and m_z' atomic d-orbitals of atoms α and β. The $\psi_{nk}(\alpha m_z)$ are the expansion coefficients of the wave function of band n at a point k for d-orbital m_z of atom α. Finally, these expansion coefficients together with the Fermi occupation numbers define the local up and down spin occupancy for atom α as

$$n_\sigma(\alpha) \equiv \sum_{n,k,m_z} w_k f_{nk\sigma} \left|\psi_{nk}(\alpha m_z)\right|^2, \tag{2.5}$$

which, when combined with the *local* atomic Stoner parameters I_α, complete the magnetic energy term of Eq. (2.1).

Once the Stoner parameters I_α for each atom are determined from the atomic environment, and the ϵ_{nk} are determined by diagonalizing the tight-binding Hamiltonian, we define the free energy of the system as the minimum of Eq. (2.1) over the chemical potentials $\mu_{\sigma=+1}$, $\mu_{\sigma=-1}$ under the constraint of preserving the correct *total* number of electrons.

2.2.2 Band structure energy

The first term of Eq. (2.1), the single-particle electronic term, represents an integral over the Brillouin zone as a weighted sum over the eigenenergies ϵ_{nk}. The integration over the Brillouin zone is carried out with a sum over a discrete set of k-points with appropriate weights w_k as chosen in the conventional way [37]. To produce the correct finite-temperature free energy of the system, the single-particle electronic term of Eq. (2.1) also includes the electronic entropy defined in Eq. (2.2). This allows us to carry out calculations at elevated electronic temperatures, a useful computational device for smoothing the Fermi surface without significantly affecting the total energy. In addition, including the entropy explicitly ensures that the familiar Fermi form of Eq. (2.3) for the fillings automatically minimizes the free energy in Eq. (2.1), a fact which we exploit below to calculate the forces. Maintaining separate Fermi levels for the up and down electrons under the constraint of the correct *total* number of spin up *and* down d-electrons, $N_d = N_{\sigma=+1} + N_{\sigma=-1}$, allows the possibility of spin polarization in the system.

While it would be reasonable to include s and p states as well, we follow Hasegawa and Pettifor and use d-orbitals only. Their work shows that a tight-binding description purely in terms of d-bands with a fixed occupation of $N_d = 7$ electrons/atom reproduces well the $P-T$ phase diagram of α-iron. In Section 2.3, we find that we also obtain such a good description by considering only d-states with a very similar population of electrons. Working with d-states only, the variables m_z, $m'_z = -2, -1, 0, 1, 2$ in Eq. (2.4) now vary over the full set of orbitals for each atom.

In expressing the k-dependent matrix elements $H_k(\alpha m_z, \beta m_z')$, particularly when evaluating forces, we find it most convenient to express the Slater-Koster angular factors explicitly in terms of the $\ell = 2$ representation of $SO(3)$, rather than employing the usual Cartesian forms of Slater and Koster [22]. (In practice, any extra computation involved in dealing with explicit rotation operators scales linearly with the number of atoms and requires far less effort than diagonalizing the resulting matrices, even for systems of relatively few atoms.) In terms of the $\ell = 2$ representation, the tight-binding Hamiltonian for d-states at point k in the Brillioun zone is then

$$\begin{aligned} H_k(\alpha m_z, \beta m_z') &= e^{\alpha \vec{k} \cdot (\vec{\tau}_\beta - \vec{\tau}_\alpha)} \times \\ &\quad [M_y e^{-i\Theta_{\alpha\beta}} M_y^\dagger e^{-i\Phi_{\alpha\beta}} \times \\ &\quad e^{-q\tau_{\alpha\beta}} K_o e^{i\Phi_{\alpha\beta}} M_y e^{i\Theta_{\alpha\beta}} M_y^\dagger]_{m_z' m_z}. \end{aligned} \tag{2.6}$$

Here, M_y is the 5×5 matrix whose columns are the $\hat{L}_y$ eigenstates expressed in the L_z basis, $\vec{\tau}_\alpha$ are the atomic positions, and $\tau_{\alpha\beta}$ is the distance between atoms α and β. The angles which appear in the rotation matrices are defined through

$$\begin{aligned} \vec{\tau}_\alpha - \vec{\tau}_\beta &\equiv \tau_{\alpha\beta}(\hat{z}\cos\theta_{\alpha\beta} + \\ &\quad \sin\theta_{\alpha\beta}\,[\hat{x}\cos\phi_{\alpha\beta} + \hat{y}\sin\phi_{\alpha\beta}]), \end{aligned}$$

in terms of which the final interatomic rotation matrices are $\Theta_{\alpha\beta} \equiv \theta_{\alpha\beta} L_z$ and $\Phi_{\alpha\beta} \equiv \phi_{\alpha\beta} L_z$, where L_z is the diagonal 5×5 matrix with diagonal elements $-2, -1, 0, 1, 2$. The terms appearing in square brackets in (2.6) thus account for the angular orientation of the two atoms. These matrix operations rotate the atoms so that the displacement between them lies along the z-direction. Finally, $e^{-q\tau_{\alpha\beta}} K_o$ is the matrix of overlap integrals at distance $\tau_{\alpha\beta}$ in this *standard* orientation. In this orientation, cylindrical symmetry ensures that only states of the same m_z will couple. Thus, K_o is a diagonal matrix with diagonal elements corresponding to $dd\sigma$, $dd\pi$, and $dd\delta$-bonding. After the usual fashion, we take these matrix elements to decay exponentially with distance, as the coefficient $e^{-q\tau_{\alpha\beta}}$ describes.

The parameters which must be determined for this part of the tight-binding Hamiltonian are thus the exponential decay factor q and the diagonal elements $dd\delta_o$, $dd\pi_o$, $dd\sigma_o$, $dd\pi_o$, $dd\delta_o$, respectively, of K_o.

2.2.3 Exchange energy

The basic Stoner form [49] describes a mean-field energetic benefit of exchange of magnitude $N_{at}Im^2/4$, where N_{at} is the total number of atoms in the crystal, m is the spin polarization per atom and I is the Stoner parameter. Although this mean-field treatment ignores thermal fluctuations of the spin density, it represents the low temperature limit of the more detailed single-band spin-fluctuation theory of Hubbard and Hasegawa [19, 18]. We thus expect an energy functional based on a Stoner approach to capture the influence of magnetic effects in complex structures below $T_f \sim 500$ K.

As we will discuss below, disorder in the liquid causes our energy functional to demagnetize at very high temperatures, reducing it in the liquid to a simple tight-binding description, which is appropriate for iron well above the Curie temperature. We thus have, within one unified framework, an energy functional for both liquid iron (high temperature demagnetized phase) and complex structures in α-iron (low temperature Stoner regime). To extend this work to the phases of iron at intermediate temperatures, one could in principle generalize the framework of [40] to inhomogeneous systems following a path analogous to what we take below.

To extend the Stoner theory beyond homogeneous bulk systems, we introduce a local approximation to the exchange energy in the same spirit as the local-density approximation[47] of density functional theory[21]. For an inhomogeneous system, we associate a separate energy contribution to exchange from each atom equal to what we would expect on a per atom basis from a homogeneous system consisting of atoms in identical environments with identical spin polarizations. The exchange energy thus becomes a sum over atoms of the product of the Stoner parameter associated with the environment of each atom and the square of the spin polarization on that atom, as appears in Eq. (2.1). The physical basis for making this approximation is

that the itinerant nature of magnetism in iron will result in smooth variations in the spin polarization, so that any "gradient" (site-to-site difference) corrections to our local Stoner approximation will tend to be small. This approach has the advantage of requiring no additional fitting beyond the form of the Stoner parameter in bulk materials.

What remains to be determined for this part of the energy functional is the dependence of the atomic Stoner parameters I_α on the atomic environment, and the number of electrons in the d-manifold, N_d.

2.2.4 Interatomic energy

The final part of our tight-binding energy functional is the repulsive interatomic potential. The role of this term is not only to embody the physical, screened repulsive interaction of the ionic cores, but also to capture those more subtle effects which our energy expression does not include explicitly. These effects include overlap repulsion, distortions in the atomic orbitals, changes in the Hartree and exchange-correlation energy due to distortions in the charge density, and band structure effects which arise from the as of yet unaccounted s and p-orbitals. Our *ansatz* is that these effects vary only mildly as the atoms move, and therefore may be captured by a simple two body form as appears in the last term of Eq. (2.1). Our choice of an exponential two-body form is governed by the fact that most of the effects which this term is to capture decay exponentially with distance. Here we follow [38] in taking the repulsive part as having a power law relationship with the hopping elements. This final part of the energy introduces only two new parameters, the overall strength of the repulsive term b and the associated decay factor p.

2.2.5 Forces

To calculate atomic forces, we note that although $E(\mu_{\sigma=+1}, \mu_{\sigma=-1})$ depends explicitly on $\tau_{\alpha\beta}$, I_α, ϵ_{nk}, $f_{nk\sigma}$ and $n_\sigma(\alpha)$, the chosen forms for $f_{nk\sigma}$ in Eq. (2.3) and $n_\sigma(\alpha)$ in Eq. (2.5), through the minimization process described at the end of Section 2.2.1,

make E stationary so that the effects of their variation with motion of the atoms need not be considered in computing the variation in total energy in Eq. (2.1). Thus, in the spirit of the Hellman-Feynman theorem, to compute the forces $\vec{F}_\ell = -dE/d\vec{\tau}_\ell$, we need to consider only changes in those terms which depend *explicitly* on the atomic locations, namely H_k, I_α, and $e^{-p\tau_{\alpha\beta}}$. The result is

$$\begin{aligned} \vec{F}_\ell &= -\sum_{nk\sigma} w_k f_{nk\sigma} < \psi_{nk} | \frac{\partial H_k}{\partial \tau_\ell} | \psi_{nk} > \\ &\quad -\frac{1}{4} \sum_\alpha \left(\frac{\partial}{\partial \tau_\ell} I_\alpha \right) (n_\uparrow(i) - n_\downarrow(i))^2 \\ &\quad -\frac{b}{2} \sum_{\alpha \neq \beta} \left(\frac{\partial}{\partial \tau_\ell} e^{-p\tau_{\alpha\beta}} \right). \end{aligned} \tag{2.7}$$

Given the electronic state of the system, each term in this expression may be evaluated directly, with no need for perturbation theory or explicit analytic understanding of the density of states.

2.3 Parameterization of the model

Eq. (2.1) is among the simplest possible expressions for the free energy functional of a system where the active degrees of freedom are bonding among the d-orbitals and the local atomic spin polarizations. With such a limited set of degrees of freedom, there are correspondingly few parameters which must be specified in the energy expression. These parameters are (1) the hopping elements of the Hamiltonian and their decay with distance, (2) the number of electrons occupying the d-manifold and the dependence of the local Stoner parameters I_α on the atomic environment, and (3) the variables b and p parameterizing the two-body repulsive interaction potential.

2.3.1 Tight-binding matrix elements

The parameterization of the tight-binding Hamiltonian for the energy expression in Eq. (2.1) proceeds from *ab initio* calculations within the self-consistent linear muffin tin orbital (LMTO) method in the atomic sphere approximation (ASA)[55].

These LMTO calculations predict the stable phase of iron as the ferromagnetic bcc phase, which is the experimentally observed stable phase for iron at $T = 0\,K$. These calculations give an equilibrium atomic Wigner-Seitz (WS) radius for the bcc phase of 2.64 Bohr (experimental value is 2.66 Bohr) and a bulk modulus within 1% of the experiment. They also show that by far the largest contribution to the total magnetic moment comes from the d-electrons. In the left panel of Figure 2-1, which gives the corresponding density of states for the d-electrons, we see that the high degree of polarization in the d-electrons originates from the opening of a pseudo-gap at a location accessible to the spin-down Fermi level. The system thus stabilizes the bcc structure by adjusting the density of states so that the Fermi level for the spin-down electrons falls in this gap.

A somewhat weaker pseudo-gap appears in the fcc density of states, but at a point too low in the band structure to attract one of the Fermi levels without placing more than five spin-up electrons in the d-band. Thus, in the end, bcc is the naturally favored structure at lower temperatures. These results all point to the fact that the physics of the d-electrons is the key to the mechanical behavior of the iron lattice.

In this work, the ratios of the Slater-Koster parameters $dd\sigma_o$:$dd\pi_o$:$dd\delta_o$ and the exponential decay factor q are adjusted to reproduce the *ab initio* density of states. We find that a choice of $dd\sigma_o$:$dd\pi_o$:$dd\delta_o = -2 : 2 : -1$ and $q = 0.63872$ Bohr^{-1} reproduces the basic shape of the LMTO-ASA density of states[55]. Finally, we adjust the absolute scale of the hopping elements to match the width of the LMTO-ASA density of states, obtaining a good fit with the choice of $dd\pi_o = 1$ Ryd.

2.3.2 Local Stoner parameters

To specify the magnetic parts of the tight-binding Hamiltonian, we must determine *both* the local Stoner parameters, I_α, *and* the total number of electrons in the d-manifold, N_d. In an ideal bulk structure, all atoms experience the same environment, so that $I_\alpha \equiv I$ takes on a constant value for a given crystal structure. However, Krasko has shown that the bulk Stoner parameter I has a mild linear volume dependence[23,

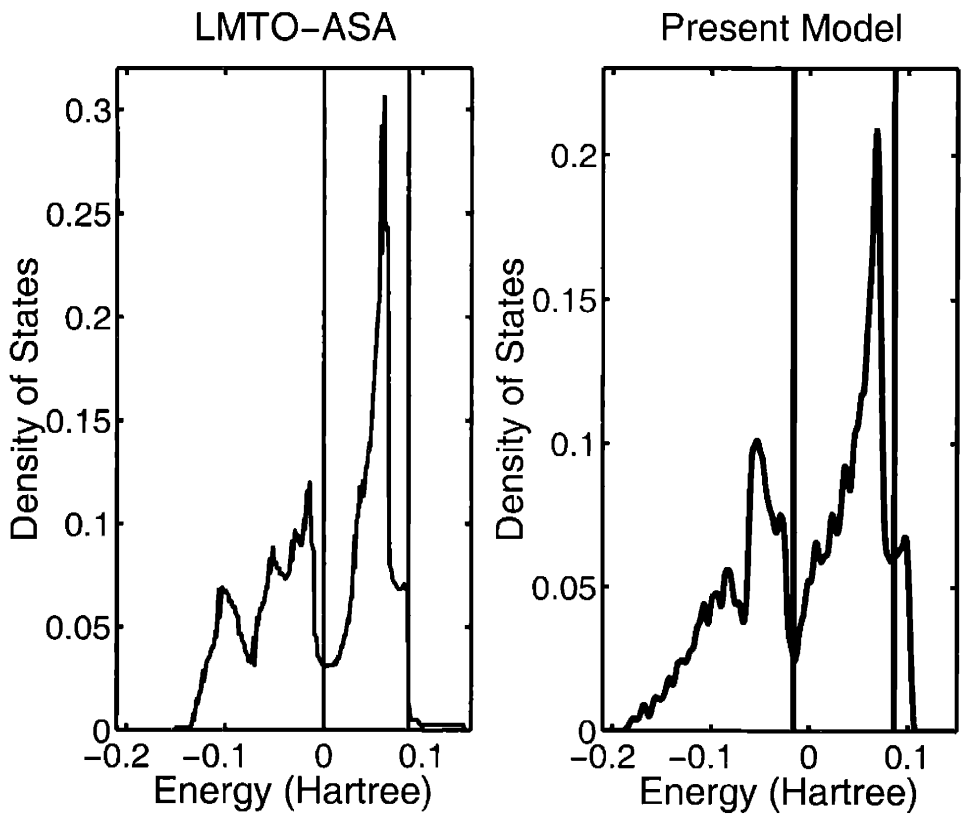

Figure 2-1: The density of states for the d-electrons in the bcc phase. The vertical lines are the Fermi levels. The left panel gives the density of states obtained in LMTO calculations [1] and the right panel is produced with our energy functional.

34],

$$I = I_o - \alpha(s - s_o), \tag{2.8}$$

where s_o and I_o are a reference WS radius and Stoner parameter, respectively, for the given structure and $\alpha = 0.01$ Hartree/Bohr.

Krasko also showed in his work that the Stoner parameters for the bcc and the fcc structures have slightly different values, $I_o^{bcc} = 0.0720$ Ryd/μ_B^2, $I_o^{fcc} = 0.0690$ Ryd/μ_B^2 at $s_o = 2.66$ Bohr. In order to yield the correct ordering of states for the bcc and fcc phases and to make the zone-edge phonon stable, we found it necessary to slightly adjust the bulk Stoner parameters to $I_o^{bcc} = 0.0770$ Ryd/μ_B^2 and $I_o^{fcc} = 0.0723$

Ryd/μ_B^2.

To go beyond the properties of bulk homogeneous systems, we generalize the Stoner parameter I of Eq. (2.8) by using *local* WS radii s_α and *local* coordination numbers Q_α in the expression

$$I_\alpha = I_{bcc} - \alpha\,(s_\alpha - s_o) - \frac{1}{4}(I_{bcc} - I_{fcc})\,(Q_\alpha - Q_o)\,, \tag{2.9}$$

where $s_o = 2.67$ Bohr is the equilibrium bcc WS radius, and $Q_o = 8$ is the bcc coordination number.

To define the local WS radii s_α, we follow the lead of Sawada [46] and define the local nearest neighbor distance R_α and coordination number Q_α through

$$R_\alpha = \frac{\sum_{\beta\neq\alpha} \tau_{\alpha\beta} e^{-\lambda_1 \tau_{\alpha\beta}}}{\sum_{\beta\neq\alpha} e^{-\lambda_1 \tau_{\alpha\beta}}}, \tag{2.10}$$

$$Q_\alpha = \sum_{\beta\neq\alpha} e^{-\lambda_2 \left(\tau_{\alpha\beta} - R_\alpha\right)^2} \tag{2.11}$$

where, as before, $\tau_{\alpha\beta}$ is the separation between atoms α and β. In this work, we choose the values $\lambda_1 \equiv 4.502319$ Bohr $^{-1}$, $\lambda_2 \equiv 10.63676$ Bohr $^{-2}$, which reproduces to within 0.01% the correct coordination numbers for the diamond structure, simple cubic, bcc and fcc lattices, when packed at the atomic density of bcc iron.

To determine the local WS radius for use in Eq. (2.9), we must first obtain the local volume per atom from Eqs. (2.10-2.11). To a first approximation, this volume is

$$V = \frac{4\pi}{3}\left(\frac{R_\alpha}{2}\right)^3. \tag{2.12}$$

To improve this approximation, we note that the ratio of the calculated volume per atom to the actual volume per atom in a perfect lattice structure should be a function of the coordination number which approaches a constant in the limit of large coordination numbers. We find that the correct WS radii, $s_\alpha = (V_{crys}\frac{3}{4\pi})^{\frac{1}{3}}$, where V_{crys} is

the volume per atom for each crystal structure mentioned in the previous paragraph, are reproduced to within 0.3% with the use of the asymptotic series

$$\frac{\frac{4\pi}{3}\left(\frac{R_\alpha}{2}\right)^3}{V_{crys}} = a + \frac{b}{Q_\alpha} + \frac{c}{Q_\alpha^2}, \tag{2.13}$$

with parameter values $a = 1.7144356$, $b = -9.094819$ and $c = 56.371742$. Using this series, the local WS radius needed in Eq. (2.9) is just

$$s_\alpha = \frac{R_\alpha}{2}\left(a + \frac{b}{Q_\alpha} + \frac{c}{Q_\alpha^2}\right)^{-\frac{1}{3}}. \tag{2.14}$$

Note that, in accord with the microscopic origins of the exchange effect, the Stoner parameter as calculated in Eq. (2.9) is a very local quantity, depending almost entirely on the locations of the nearest-neighbor atoms.

Finally, we set the number of electrons in the d-manifold to $N_d = 6.7$ electrons/atom [55]. With this value for the occupancy, the Fermi level for the spin-down electrons falls precisely into the pseudogap in the density of states for the bcc structure, thereby stabilizing the bcc phase and reproducing the physical behavior observed in the *ab initio* calculations. Note that the filling $N_d = 6.7$ electrons/atom is in good agreement with the value of $N_d = 7.0$ electrons/atom used with success in [40].

2.3.3 Interatomic potential

With the electronic parts of the energy expression Eq. (2.1) fully specified, we now adjust the parameters describing the empirical two-body repulsive interaction in order to capture any residual effects not described in the electronic part of the energy. We adjust the two parameters b and p defining the potential to reproduce the experimental values for equilibrium lattice constant and bulk modulus for the bcc phase of iron. The resulting values for p and b are 2.2355 Bohr^{-1} and 872.5174 Ryd, respectively [55]. The power law relationship between the tight-binding matrix elements and the interatomic repulsive part then has an exponent $\lambda \equiv p/q$ which leads to a *normalized*

	E_{gb} [erg/cm^2]	E_{ex} [erg/cm^2]	Δm	ΔI_{min}
$\Sigma5(310) < 001 >$	870 (770[a]) (1300[b])	-1300 (23 %)	10% (8%[c])	2%
$\Sigma3(112) < 110 >$	320 (300[b])	-900 (37 %)	6%	1%
$\Sigma3(111) < 110 >$	900	-4500 (30 %)	16% (15%[d]-18%[e])	4%
$\Sigma9(114) < 110 >$	600 (770[a]) (1450[b])	-1500 (35 %)	15%	2%

Expt: [a][52], EAM: [b][28]; *Ab initio*:[c][9], [d][24], [e][35].

Table 2.1: Summary of grain boundary results: boundary formation energy [E_{gb}], exchange contribution to the energy [E_{ex}], percentage change in magnetic moment on the boundary plane [Δm], percentage increase in Stoner parameter [ΔI_{min}]. Results of other studies are given in parentheses.

hardness [38] $\alpha_h \equiv (\lambda - 1)/\lambda \approx 0.7$, well in line with the values of about 2/3, usually observed for transition metals [38].

2.4 Results

2.4.1 Extended defects in α-iron

We now consider symmetric tilt grain boundaries, one of the fundamental topological excitations of crystalline iron which govern mechanical response in general and intergranular cohesion and microstructure in particular. We carried out our calculations using periodic boundary conditions in supercells containing two oppositely oriented grain boundaries separated by at least eighteen layers of atoms and performed full structural and supercell lattice relaxations with five layers of atoms (equidistant from the boundaries in the cell) frozen at the bulk lattice spacing.

Table 2.1 summarizes the results. The first column identifies the boundaries in our study. The second column gives the interfacial energy for each. The interfacial energies show that our model correctly identifies the lowest energy boundary as the naturally occurring $\Sigma3$ (112) $< 110 >$ with an energy significantly lower than all other boundaries in our study. EAM calculations (in parentheses) also produce a very similar energy value for this coherent twin $\Sigma3$ (112) boundary, which is not surprising

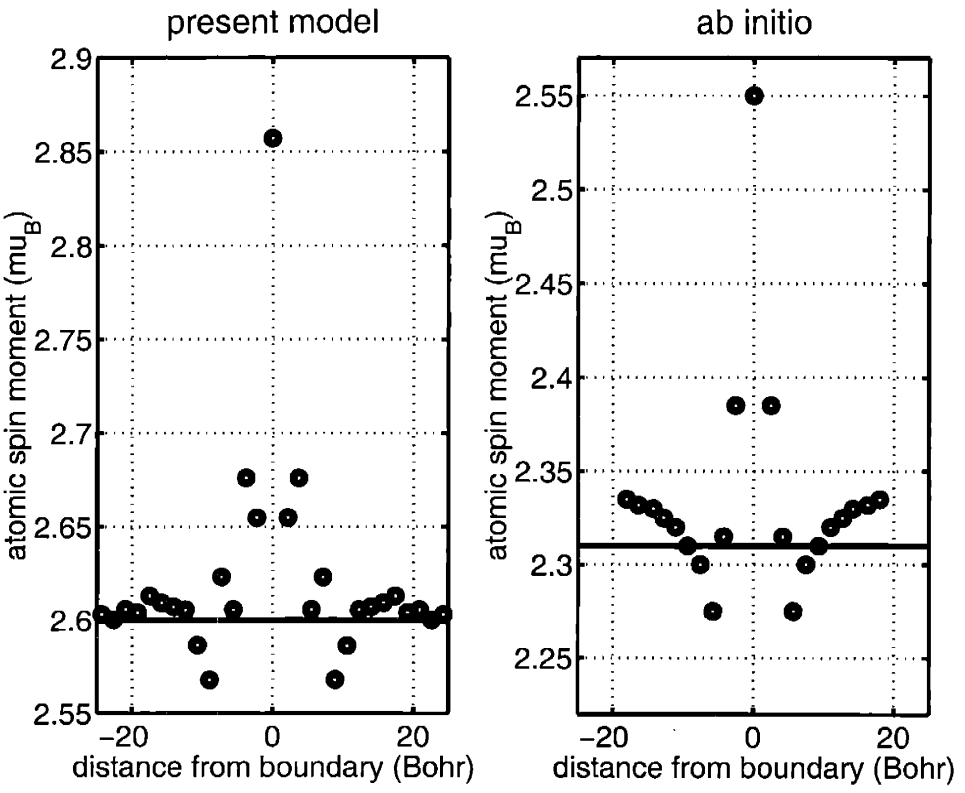

Figure 2-2: Atomic spin moment distribution in the vicinity of the $\Sigma 5(310)$ grain boundary. The left panel gives the distribution obtained with the present tight-binding energy functional, the right panel gives *ab initio* results of [9].

since this particular boundary is very bulk-like, and EAM potentials are traditionally fit to reproduce well the properties of bulk iron well. A more objective comparison can be made for the $\Sigma 5$ (310) $<$ 001 $>$ and $\Sigma 9$ (114) $<$ 110 $>$ boundaries, with structures which differ significantly from bulk material. While experimental studies predict a mean typical boundary energy of 770 erg/cm^2[52], EAM overestimates this value by a factor of two whereas our model produces results in much better accord with the experiment.

The third column of the table gives the contribution to the boundary energies from the exchange term. The large negative values of this contribution indicate that the exchange interaction, not accounted explicitly in the EAM, significantly stabilizes the boundaries and enhances inter-granular cohesion by lowering the boundary energies. To understand the physical origin of this effect, we now analyze the individual

contributions to the last term in Eq. (2.1), namely the Stoner parameters and the atomic magnetic moments. Because we treat these two effects locally, a local change in either of them could affect the exchange energy. Our calculations show that for each of the boundaries we studied, there is a $6-16\%$ enhancement of the magnetic moments on the symmetry plane (fourth column of Table 2.1, which is in excellent agreement with the available *ab initio* predictions[24, 35] (listed in parentheses)). The local Stoner values also increase (thereby further stabilizing the boundaries) but only by about $1-4\%$ (fifth column of the table) so that this is not the controlling effect.

To further understand this magnetic enhancement, Figure 2-2 compares the magnetic moment distribution for the $\Sigma 5(310)$ grain boundaries, obtained with the present tight-binding energy functional and *ab initio* calculations [9]. Both sets of results show a fractional enhancement of the moments on the boundary (10% with the present model, 8% in *ab initio* calculations), followed by a spin-depression echo in the vicinity of the boundary and an eventual healing back to the bulk value. While the spin enhancement on the boundary is similar, our calculations place the location of the spin depression somewhat farther away from the symmetry plane of the boundary. Nonetheless, we find this remarkable level of agreement with the *ab initio* data for even subtle effects such as the spin distribution. Given that our functional is extremely simple and fitted to only bulk phase information, this result strongly supports the soundness of the functional and its capability of capturing the correct microscopic physics.

This spin enhancement, which we have seen to be the dominant contribution stabilizing the boundaries, can be understood in terms of a simple band-structure effect. First, we note that it is the states in the energy range near the band center control the net magnetic moment because states with energy below both Fermi levels $\mu_{\sigma=-1}$ and $\mu_{\sigma=+1}$ are filled equally with up and down spins and contribute nothing to the net moment as do the completely empty states with energies above both Fermi levels. Combining this with the fact that such mid-band states tend to localize where the bands spread less due to disruption in the bonding, we indeed expect the spin moments to concentrate on the the grain boundaries.

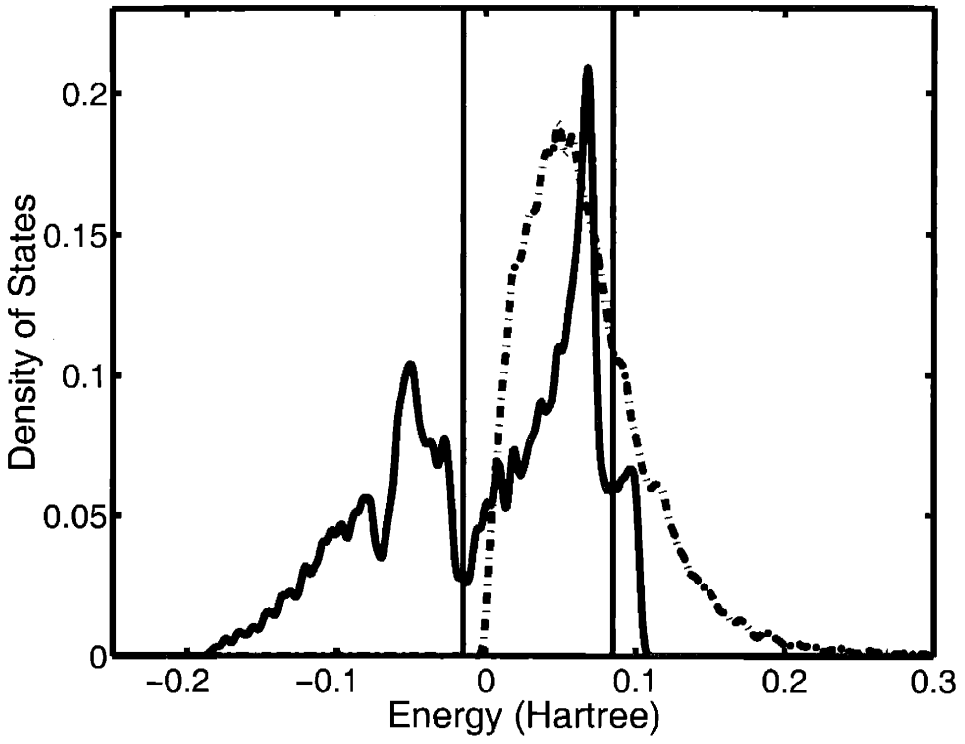

Figure 2-3: DOS for bulk (solid line) and LDOS for grain boundary layer (dashed line) for $\Sigma 5(310)$ boundary.

We have confirmed the latter of the above effects leading to spin enhancement on the boundaries by direct inspection of the electronic states. Also, by comparing the local density of states (LDOS) for the symmetry plane atoms with the LDOS of the bulk atoms in Figure 2-3, we can clearly see that there is an enhancement of the LDOS for atoms on the boundary plane in the energy range between the Fermi levels.

Table 2.2 summarizes our results for the structural relaxation associated with a number of grain boundaries. These results indicate a general trend toward outward motion of the layers neighboring the symmetry plane, which tends to further disrupt the bonding and enhance the magnetic moment and thus the energetic benefits of exchange. In the case where we have *ab initio* data, for the $\Sigma 3(111)$ boundary, we find good agreement in the outward expansion of the layers of atoms neighboring the boundary plane.

Table 2.3 makes a detailed comparison of our results and the available *ab initio*

	Σ5(310)	Σ3(112)	Σ3(111)	Σ9(114)
Δz_{Layer2}	0.52	0.09	0.68 (0.5^e-0.8^f)	0.33
Δz_{bulk}	0.36	0.01	0.55	1.23

Ab initio: [e][36], [f][35]

Table 2.2: Outward motion of planes immediately neighboring the boundary [Δz_{Layer2}] and the total outward motion of the bulk slab [Δz_{bulk}] in Bohr for various boundaries.

structural predictions for the Σ3(111) boundary[35, 36]. In this table, a shift of zero indicates that the corresponding atomic plane rests at the position which one would expect in an unrelaxed CSL (coincident site lattice) boundary. The final column of the table gives the displacement of the planes far into the bulk, which represents one-half of the net outward expansion associated with the grain boundary. In interpreting the results in the table, it is important to note that the data in each row associate with different boundary conditions. The data in the first row is from an isolated cluster with its outer atoms held fixed [35], which artificially hampers the outward relaxation of the boundary. The data in the second row are for an infinite periodic slab exposed to vacuum on both sides [36], which, with the tendency of metallic atoms to seek a bulk-like environment, also tends to artificially hamper outward motion. Finally, our results in the third row were from calculations in which we employed periodic boundary conditions to large cells (12 layers of atoms between grain boundaries), performed full lattice relaxation, and thereby allowed the boundary to relax outward naturally.

Despite the apparent differences in the applied boundary conditions, we find good agreement between our results and the *ab initio* conclusions. In particular, Table 2.3 shows the same trends in the layers near the boundary (Layers 2-5): Layer 2 (which neighbors the symmetry plane, and is least effected by the boundary conditions) moves significantly outward, and Layers 3 and 4 move less (or inward in the case of the cluster calculation). Layer 5, whose atoms are directly in line with those of Layer 2, also shows a noticeable outward motion. For the outer layers, our results quickly revert to the bulk inter-layer spacing, as indicated by the nearly constant

Δz (Bohr)	L2	L3	L4	L5	L6	L7	Bulk
Cluster	0.78	-0.81	-0.00	0.78	-0.81	-0.00	N/A
Free Slab	0.54	0.24	0.18	0.23	0.18	0.10	??
TB	0.68	0.20	0.32	0.59	0.50	0.51	0.55

Table 2.3: Displacement of the atomic layers (L2-L7) from their geometric grain boundary positions for the $\Sigma 3(111)$ boundary.

shifts for layers 6, 7 and 8. For these outer layers 6-8, the *ab initio* results give reduced displacement, a direct artifact of the employed boundary conditions.

In summary, we find the following universal trends for the symmetric tilt grain boundaries in iron: (a) the exchange contribution to the total energy stabilizes the grain boundaries and increases inter-granular cohesion; (b) most of the contribution to the exchange energy comes from the enhancement of magnetic moments on and in the vicinity of the boundary plane, a band structure effect arising from the more open environment of the boundary plane; (c) our model correctly describes, both qualitatively and quantitatively, the outward relaxation of atomic layers neighboring the boundaries.

2.4.2 Liquid phase

In the liquid phase, well above the Curie temperature, magnetic order is lost, and exchange effects become far less important in iron. Although our tight-binding energy functional does not describe spin correlation effects, which are quite important at intermediate temperatures, disorder in the liquid causes our model to demagnetize. This effect reduces our energy functional to a non-magnetic tight-binding description appropriate for the liquid. We now explore how well this description captures liquid phase behavior.

To predict the properties of liquid iron, we carried out molecular dynamics studies using the Verlet algorithm[50] with a time step of 5.16 fs (about $\frac{1}{20}$ the Debye period). We employed a cubic supercell of 54 atoms in a fixed volume of $(16.272 \text{ Bohr})^3$ with Brillouin zone sampling at 144 k-points, and ran constant volume simulations at

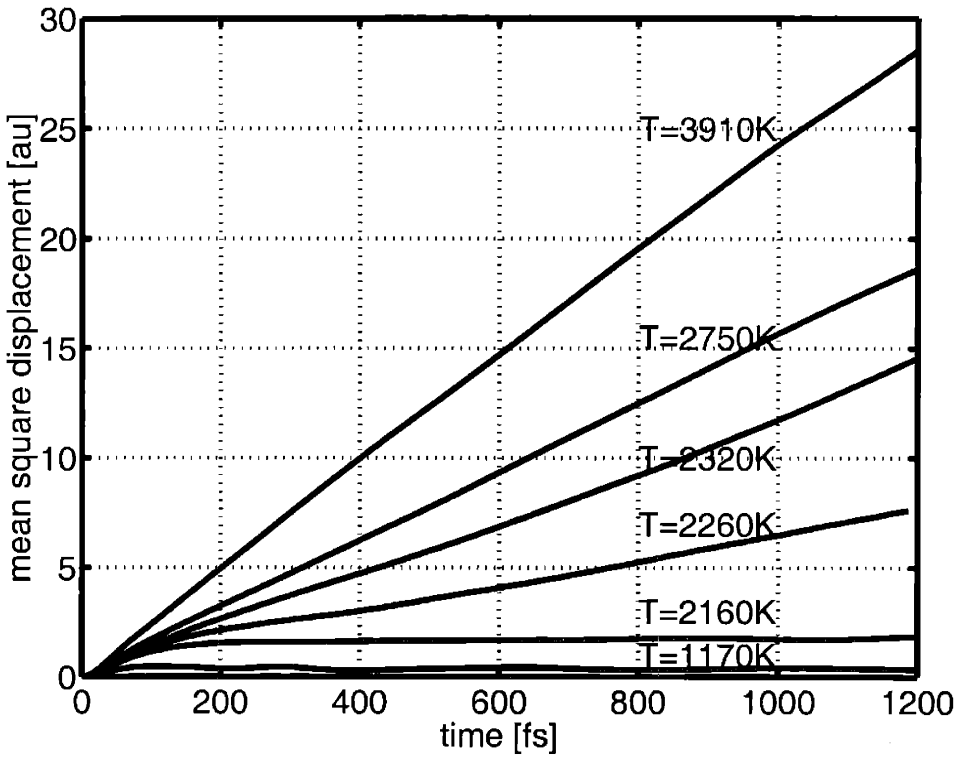

Figure 2-4: Atomic mean square displacement as a function of time for different temperatures.

1170 K, 1810 K, 2160 K, 2260 K, 2320 K, 2670 K, 2750 K, 3910 K and 4010 K. Even in this highly anharmonic regime, the total energy in all our runs was conserved to better than 2 % over 1.2 ps with no detectable systematic drift.

Figure 2-4 presents our results for the average mean square displacement of the atoms in our calculation as a function of simulation time. For all temperatures, the mean square displacement begins with a quadratic ideal-gas like (ballistic) regime during the first $\sim$ 1/4 Debye period. At the lower temperatures, the mean square displacement reaches an asymptotic value at long times. This indicates that the atoms simply vibrate about their equilibrium lattice positions as is the characteristic of a solid. The intermediate and higher temperature data, however, exhibit classic linear diffusion behavior at long times, the signature of liquid behavior. The transition between these regimes sets the *constant volume* melting temperature of our tight-binding energy functional to somewhere between approximately 2160 K and 2260 K.

In order to compare this prediction of the *constant volume* melting point with available experimental data, we begin by noting that the thermodynamic relationship between pressure and temperature at constant volume is $dP/dT|_V = \alpha/\kappa$, where α and κ are respectively the thermal expansion coefficient and the isothermal compressibility, so that the $P - T$ curve for the solid at constant volume is

$$P = \frac{\alpha}{\kappa} T, \tag{2.15}$$

Next, the phase boundary between solid and liquid phases is described by the relation

$$P = \frac{L_f}{T_m \left(\frac{1}{\rho_L} - \frac{1}{\rho_S}\right)} (T - T_m), \tag{2.16}$$

where L_f is the latent heat of fusion, T_m is the melting temperature at constant pressure, and ρ_L and ρ_S are the densities for the liquid and the solid phases, respectively. Finally, the intersection of Eqs. (2.15) and (2.16) gives the melting temperature at constant volume in terms of parameters which are all known experimentally and yield a value of 2350 K. The prediction of our model of 2160 K–2260 K is within 8% of this value, an excellent level of agreement.

Finally, we may extract the diffusivity and the activation energy for self-diffusion in the liquid from our data. The diffusivity is the asymptotic slope of the mean square displacement at longer times. Figure 2-5 shows an Arrhenius plot of our extracted diffusivity as a function of inverse temperature. To extract the activation energy, we note that in terms of microscopic parameters, the diffusivity is

$$D = nae^{-\beta E_A}, \tag{2.17}$$

where a is the lattice constant, E_A is the activation energy for self-diffusion, and n is a constant of order unity. The slope of the Arrhenius plot gives our calculated value of the activation energy as 0.31 eV, within 0.2 eV of the experimental result of 0.53 eV [53]. Given the simplicity of our model and that full-blown *ab initio* calculations regularly give errors on the order of 0.1 eV for such barriers, we find this agreement

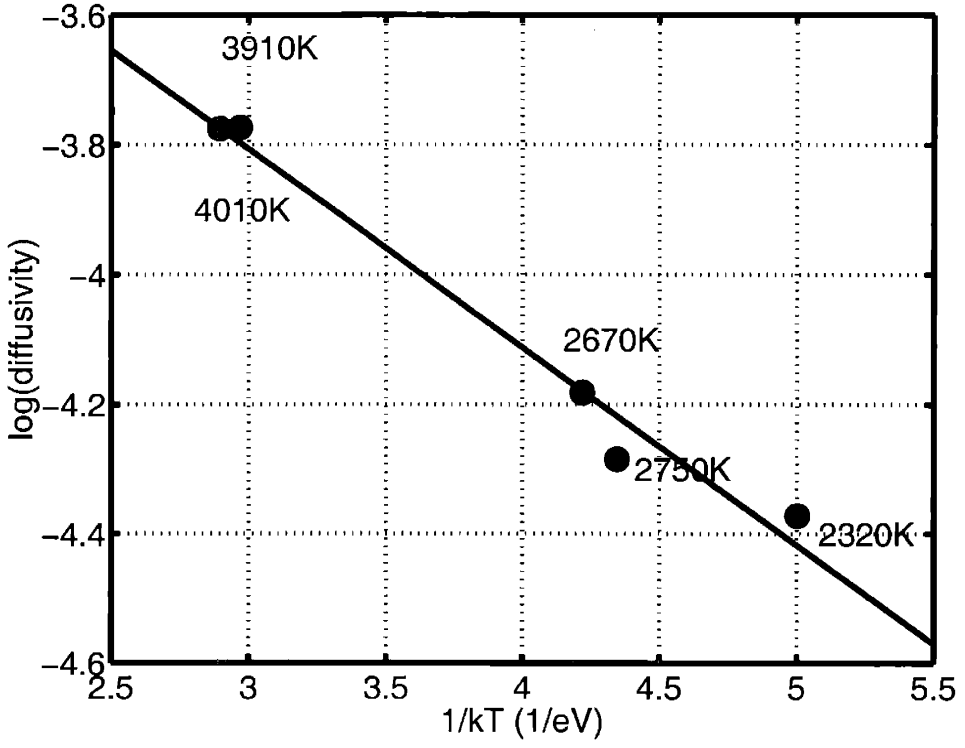

Figure 2-5: Arrhenius plot of the diffusivity of iron. The slope of the line is the activation energy for self-diffusion in the liquid.

to be very good.

2.5 Conclusion

We have identified the active microscopic degrees of freedom which control the macroscopic behavior of inhomogeneous iron, bonding among the atomic d-states and the atomic spin moments. From these degrees of freedom, we have shown that it is possible to build a coarse-grained Hamiltonian which provides an accurate understanding of a wide array of physical properties of iron at both room temperature and in the liquid. Below the $T_f \sim 500$ K shoulder of [40] where spin fluctuations become important, such a description captures the physics of the magnetic moments of bcc iron, the relative ordering and elastic properties of the bulk phases, and the behavior of

symmetric tilt grain boundaries. Our results from the grain boundary study are in good quantitative agreement with the experimental and *ab initio* data for the energetics of the defects. Analyzing the behavior of the aforementioned active degrees of freedom in the vicinity of the grain boundaries gives insight into the stabilizing role of exchange interaction and the forces driving the relaxation of the atomic structure. Finally, near and above the melting point, our tight-binding Hamiltonian also describes well the liquid state, giving impressive agreement with experiment for both the melting point at constant volume and the activation energy for self-diffusion.

Chapter 3

Atomic-level physics of grain boundaries in bcc metals: molybdenum as a case study

Abstract:

We present a systematic trend study of the symmetric tilt grain boundaries about the $\langle 110 \rangle$ axis in molybdenum. Our results show that multiple structural phases, some incorporating vacancies, compete for the boundary ground state. We find that at low external stress vacancies prefer to bind to the boundaries in high concentrations, and moreover, that external stress drives structural phase transitions which correspond to switching the boundaries on and off as pipe-diffusion pathways for vacancies.

3.1 Introduction

Molybdenum, with its high melting point and relatively inert chemical nature, is often considered for high-temperature structural applications, but its extreme brittleness limits its usefulness. Quasi-static bicrystal stress-strain experiments[57, 59] demonstrate that this brittleness is an intrinsic property of the material and largely unrelated to the presence of impurities. Similar studies observe inter-granular fracture at about 1.7 GPa, suggesting that this brittleness arises from weak inter-granular cohesion along the grain boundaries[58]. These results also show that impurity concentration does affect inter-granular cohesion, but only as a secondary effect. Spallation experiments, on the other hand, show contradictory results. Large-grained ($\sim$1 mm) samples have been observed to exhibit *trans*-granular spall at what the authors of that study consider to be relatively low stresses ($\sim$2.5 GPa)[60], whereas spallation in fine-grained ($\sim$5 μm) samples has been observed to be highly *inter*-granular in nature and to occur at much higher stresses (15-25 GPa)[33]. In an attempt to shed light on this complex situation, we have investigated the microscopic physics of these boundaries. In particular, we have carried out a detailed, atomic-level trend study of the behavior and structure of the low energy phases of these boundaries and the transitions among these phases.

This study reveals new physics in the interaction of the grain boundaries with vacancies. The traditional mechanisms of interplay between vacancies and grain boundaries include pipe diffusion of vacancies along the boundary[10, 11, 12], and absorption and emission of vacancies during continuous climb of primary or secondary dislocations[6, 17, 26, 5]. We find, in addition, that boundary vacancies prefer to collect together at high densities on the boundary plane. Our results also indicate that grain boundaries can either emit or absorb large concentrations of vacancies into the surrounding bulk while undergoing structural phase transitions under applied stress. Our focus in the present study is on the particular system of symmetric tilt boundaries around the $\langle 110 \rangle$ axis in molybdenum, which are known to dominate the recrystallization texture of this material[58].

3.2 Procedure

The heavy computational demands of full-blown *ab initio* electronic structure calculations [14] and semi-empirical tight-binding models [8, 39, 27, 16, 1] restrict their use to the study of relatively small systems and relatively few configurations. In order to understand complex processes such as fracture, dislocation migration and inter-granular cohesion, computationally more feasible empirical potentials must be used. Moriarty has developed such an empirical model based on a multi-ion interatomic potential developed from first principles generalized pseudopotential theory[29]. The resulting model generalized pseudopotential theory (MGPT) potential, which has been thoroughly described in literature[29, 30, 31, 32, 41], successfully predicts the cohesive, structural, elastic, vibrational, thermal and melting properties of molybdenum[31], as well as the ideal shear strength and self-interstitial and vacancy formation energies[32]. We use this potential throughout this work.

We would like to note here that even though the MGPT formalism has been generalized to include local volume changes[41] of potential importance in deformation, defect and surface calculations, these effects have been shown to be small for bulk defects ($\sim$ 0.01 eV vacancy formation energies in bcc metals[32, 41]). Accordingly, we here use the simpler form of the MGPT potential as Xu and Moriarty have done in their work on dislocations[32].

Focusing on the $\langle 110 \rangle$ symmetric tilt boundaries, we consider $\Sigma 3(112)$ and $\Sigma 9(114)$, which are among the lowest in energy, and $\Sigma 3(111)$, $\Sigma 9(221)$, $\Sigma 11(113)$ and $\Sigma 11(332)$ as examples of boundaries with higher energies. To study the physics of these boundaries, which reside in bulk material, we employ periodic boundary conditions as the most natural. To minimize boundary-image interactions, we always maintain at least seventeen layers of atoms between boundaries in our supercells.

Determination of the ground state and the low energy excited state structures in principle requires the exploration of the phase space of all possible configurations, which is an impractical task without taking into account some basic physics. The primary consideration we use to restrict this phase space is that, due to the relatively

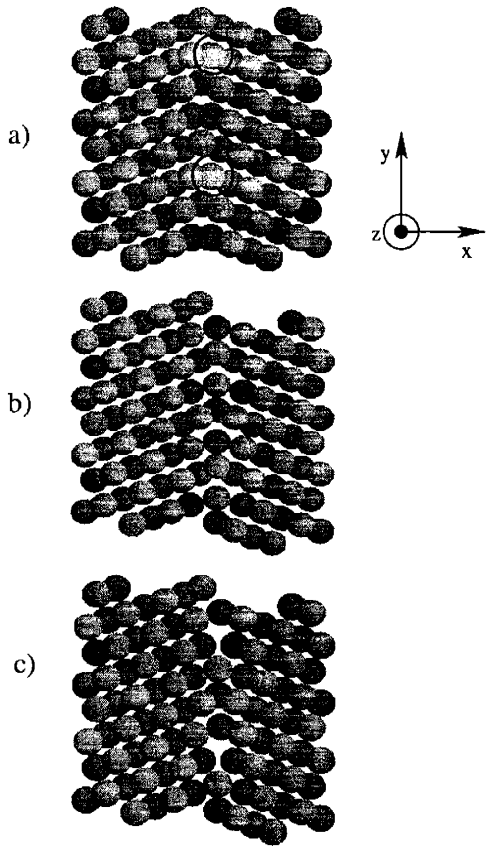

Figure 3-1: Structural phases of the $\Sigma 9(114)$ grain boundary: (a) naïve CSL boundary, (b) relaxed full-material boundary, (c) relaxed vacancy phase boundary. (To aid visualization, atoms from the two cubic sublattices are colored separately, light and dark.)

strong directional bonding in molybdenum and similar bcc metals, the structure of the grain boundaries tends to preserve the *internal* topology of individual grains. Under this restriction, there remain then only three considerations for each boundary: (1) possible addition and removal of atoms to and from the faces of the grains at the boundary, (2) displacement of the grains relative to one another, and (3) relaxation of the internal atomic coordinates.

For the first consideration, the fact that the interstitial energy in molybdenum ($\geq$ 10 eV) is much larger than the vacancy energy (3 eV)[32] indicates that insertion of additional material at the boundary leads to unlikely high interfacial energies. We therefore concentrate only on the *removal* of atoms at the boundary. Direct

calculations with the MGPT potential reveal that the most favorable sites for atom removal are in the vicinity of the boundary. It turns out that, because the atoms in the planes adjacent to the boundary plane (indicated by circles in Figure 3-1a) pack closely together, these sites are the energetically most favorable for vacancy formation.

This leads us to consider the following structural phases for the boundaries in our study: grains joined with the amount of material expected from the *naïve* coincident site lattice (CSL) construction ("*full-material phase*"), and boundaries where we remove atoms from the circled sites in Figure 3-1a, which shows this construction. Below, we find that binding energy per boundary vacancy is higher when vacancies collect together at high density on the boundaries. Therefore, we first concentrate on boundaries with high vacancy densities. Because removal of an entire plane of atoms near the boundary is topologically equivalent to the initial "full material" phase under appropriate relative displacement of the grains, we first focus on the phase where we remove one half-plane of atoms from the layer adjacent to the boundary ("*vacancy phase*").

To determine the ground state of the above two structural phases, we next turn to the second consideration above, the relative shifts of the grains. The displacement-shift complete (DSC) cell, which we explore on a 16×16 sampling grid (which reduces to 4×4 by symmetry), contains all possible unique relative planar shifts of the grains. We then address the third consideration by performing full relaxations of the internal grain coordinates in order to determine the most favorable DSC shift. To complete our search, we then apply a series of external strains which cover the full range of stresses explored below, and we perform full internal relaxations for each strain. This allows us both to identify the ground state and to study the response of the boundary to externally applied strain. We note here that this extensive survey requires force and energy calculations of approximately 400,000 configurations, and would not be feasible to carry out with electronic structure techniques.

To confirm the effectiveness of this survey in identifying ground state structures, we repeat the above procedure with supercells in which we remove an entire plane of

Boundary	$\mathcal{U}_o$ [mJ/m^2]	Δx [Å]	Δy [Å]	Δz [Å]	$\Delta(1/k)$ [mJ/m^4] $\times 10^{-20}$	$\Delta(a)$ [m^7/mJ^2] $\times 10^{-30}$
Σ3(112)	610	0.1	0.3	0.0	900	1
Σ3(111)	2020	0.5	0.3	0.0	4770	-306
Σ9(114)	1730	0.5	0.1	0.0	3410	-27
Σ9(221)	2180	0.4	0.1	0.0	100	15
Σ11(113)	1740	0.5	0.2	0.0	1460	-15
Σ11(332)	2160	0.4	0.5	0.0	580	-29

Table 3.1: Full-material phase: energies ($\mathcal{U}_o$), perpendicular expansions (Δx), shifts (Δy and Δz) relative to the CSL construction, compliances ($\Delta(1/k)$) and anharmonic coefficients (Δa) relative to bulk. Coordinates are as defined in Figure 3-1.

atoms from the boundary. For all six boundaries in our study, our procedure indeed identifies the appropriate shift to recover the initial, topologically equivalent ground state found for the full-material phase before the removal of the plane of atoms.

3.3 Results

3.3.1 Low Energy Phases

Our results reveal several general trends in the physics of the $\langle 110 \rangle$ tilt grain boundaries in molybdenum. As a specific example, consider the Σ9(114) boundary, which Figure 3-1 shows. Figure 3-1a shows the naïve CSL construction of the full-material phase, whose ground state as identified through our procedure, appears in Figure 3-1b. We find that this phase lowers its energy through both a perpendicular expansion of the boundary and inter-granular shifts parallel to the boundary, both of which tend to increase the local volume for the closely packed atoms near the boundary plane, restoring them to a more bulk-like environment.

Table 3.1 shows that the outward expansion is a general trend among all grain boundaries in our study and that shifts occur along the boundary in the direction perpendicular to the tilt axis ($y-$direction, Figure 3-1) to allow for a more bulk-like local environment. We find no significant shifts along the tilt axis ($z-$direction,

Boundary	$\mathcal{U}_o$ [mJ/m^2]	Δx [Å]	Δy [Å]	Δz [Å]	$\Delta(1/k)$ [mJ/m^4] $\times 10^{-20}$	$\Delta(a)$ [m^7/mJ^2] $\times 10^{-30}$
$\Sigma 3(112)$	2130	-0.1	0.4	0.0	3030	-24
$\Sigma 3(111)$	2450	0.1	0.3	0.0	1440	-62
$\Sigma 9(114)$	2360	0.3	0.1	0.0	7250	11
$\Sigma 9(221)$	2380	0.3	0.9	0.0	2210	17
$\Sigma 11(113)$	2070	0.3	0.8	0.0	2370	28
$\Sigma 11(332)$	2590	0.2	0.4	0.8	2400	26

Table 3.2: Vacancy phase: energies ($\mathcal{U}_o$), perpendicular expansions (Δx), shifts (Δy and Δz) relative to the CSL construction, compliances ($\Delta(1/k)$) and anharmonic coefficients (Δa) relative to bulk. Coordinates are as defined in Figure 3-1.

Figure 3-1) for this phase of any of the boundaries. The next column of the table gives the mechanical compliance ($1/k$) of each boundary, where k is determined from the quadratic response of the energy per unit area per boundary as the cell expands. Finally, the last column of the table lists $a \equiv \alpha/k^3$, where α captures any non-quadratic behavior in the energy expression,

$$\mathcal{U} = \mathcal{U}_o + \frac{1}{2}k(x - \Delta x)^2 + \frac{1}{6}\alpha(x - \Delta x)^3 + \ldots \tag{3.1}$$

where x is the expansion of the cell, and Δx and $\mathcal{U}_o$ are the relaxed perpendicular expansion and boundary energy given in the table, respectively. The table lists the difference between $1/k$ and a for the boundary and for the same cell filled with bulk, as it is these differences which define the response of the boundary, *independent* of the bulk content of the cell.

Turning now to the vacancy phase, Figure 3-1c shows the results of our ground-state search for the $\Sigma 9(114)$ boundary as formed by removing the circled atoms from Figure 3-1a. We again find grain-shifting as well as local internal relaxations to create more bulk-like local atomic environments, as Table 3.2 summarizes. The perpendicular shift is always *inward* compared to the ground state of the full-material phase, so as to close the material void associated with the vacancies. Finally, we frequently

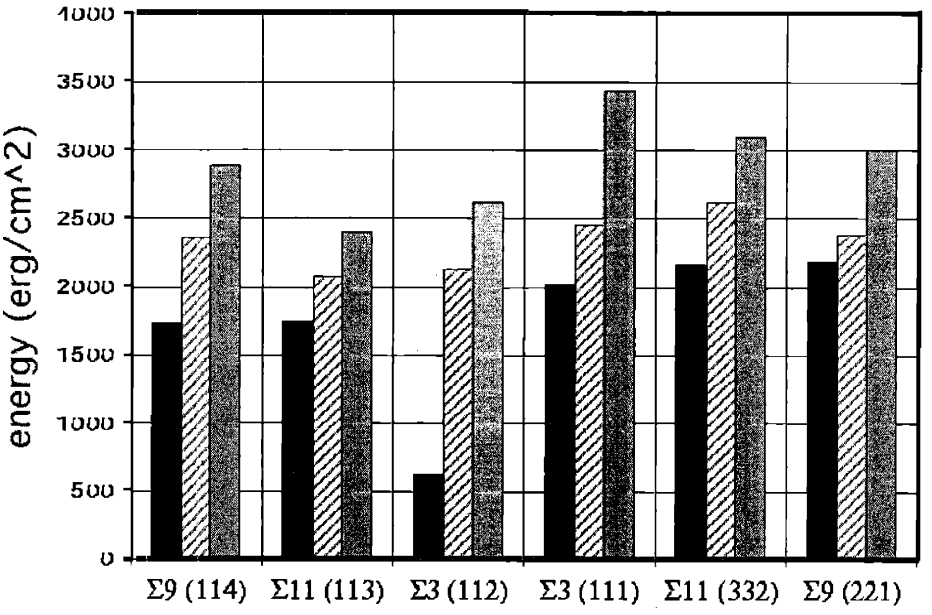

Figure 3-2: Energetics of grain boundary phases: full-material phase (black bars), vacancy phase (hatched bars), bulk-vacancy phase (gray bars).

find for the vacancy phase, even for the highly stable $\Sigma 3$'s, parallel shifts relative to the full-material phase which produce more natural bonding arrangements for the boundary to accommodate the vacancies. This tendency for accommodation is so strong as to induce the only shift along the tilt axis we observe in this study, for the vacancy phase of the $\Sigma 11(332)$ boundary.

Figure 3-2 compares the ground-state boundary energies of the various phases. In all cases, we find the full-material phase (black bars) to be lower in energy than the vacancy phase (hatched bars), although often not by far. As in the experimental case, MGPT predicts the lowest ground state interfacial energy to be for the naturally occurring twin $\Sigma 3$ (112) boundary[58]. Moreover, apart from this twin, all remaining ground state boundary energies are fairly constant (within 25%), as also found in experiment (within 30%[58]).

Figure 3-2 presents another relevant comparison. To transform physically into the full-material phase, the vacancy phase must first expel its vacancies into the sur-

Boundary	$\mathcal{U}_o$ [mJ/m^2]	Δx [Å]	$\Delta(1/k)$ [mJ/m^4] $\times 10^{-20}$	$\Delta(a)$ [m^7/mJ^2] $\times 10^{-30}$
Σ3(112)	130	-0.003	1050	-1
Σ3(111)	100	-0.002	870	-117
Σ9(114)	80	0.003	500	-32
Σ9(221)	60	-0.001	470	-0
Σ11(113)	50	-0.001	130	-5
Σ11(332)	60	-0.005	180	-39

Table 3.3: Isolated vacancy enthalpy information for each boundary orientation. Results are expressed for the number of vacancies per unit area of the corresponding boundary-vacancy phase. Lattice expansion Δx, compliance $\Delta(1/k)$ and anharmonic Δa information are for longitudinal strain perpendicular to the boundary plane.

rounding bulk material. Thus, when considering transitions, the relevant comparison is between the vacancy phase and a third phase, which consists of the full-material phase plus the corresponding number of vacancies in the surrounding bulk material ("*bulk-vacancy phase*"). To describe the enthalpies of isolated vacancies in bulk under external stresses applied in the direction corresponding to the orientation of each boundary, we repeat the procedure from Section 3.2 with the same supercells, but filled with bulk material and a single vacancy. Table 3.3 summarizes the results. The resulting energies may then be added to the full-material phase to produce the energy of the bulk-vacancy phase (gray bars in Figure 3-2). Figure 3-2 shows that, although creation of vacancies on the boundary always increases the boundary energy, the energy for creating the corresponding number of vacancies in the bulk is always higher. Our results therefore are consistent with the fact that the boundaries act as reservoirs for vacancies, as occurs during pipe diffusion.

To verify, as mentioned above, that boundary vacancies indeed prefer to cluster together, we have also considered boundaries with nearly isolated vacancies within our supercell approach. Table 3.4 presents energy, displacement, compliance, and anharmonic results for boundaries from supercells with low vacancy densities ("*dilute-vacancy phase*"). In these calculations, the vacancy concentration (3.3%) is one fifteenth that of the vacancy phase. Table 3.5 compares the boundary-vacancy binding

Boundary	$\mathcal{U}_o$ [mJ/m^2]	Δx [Å]	Δy [Å]	Δz [Å]	$\Delta(1/k)$ [mJ/m^4] $\times 10^{-20}$	$\Delta(a)$ [m^7/mJ^2] $\times 10^{-30}$
Σ3(112)	720	0.1	0.3	0.0	950	-22
Σ3(111)	2076	0.5	0.3	0.0	2060	2
Σ9(114)	2360	0.4	0.1	0.0	3520	-10
Σ9(221)	2200	0.3	0.1	0.0	260	-69
Σ11(113)	1900	0.5	0.2	0.0	1900	-3
Σ11(332)	2250	0.4	0.5	0.0	990	-125

Table 3.4: Dilute-vacancy phase: energies ($\mathcal{U}_o$), perpendicular expansions (Δx), shifts (Δy and Δz) relative to the CSL construction, compliances ($\Delta(1/k)$) and anharmonic coefficients (Δa) relative to bulk. Coordinates are as defined in Figure 3-1.

energies for the vacancy and dilute-vacancy phases. As the larger binding energies reflect, the concentrated phase (*vacancy phase*) is more stable. This added stability appears to arise from the structural relaxation through parallel shifting of the grains, which is made possible by the high density of vacancies. Finally, we observe that in the extreme case of the Σ11 boundaries, vacancies do not even bind to the boundary at low concentrations.

3.3.2 Phase Transitions

Three trends which the preceding results exhibit can be expected from general, material-independent considerations: (1) that the boundaries present preferred binding sites for vacancies because they disrupt the bulk bond-order, (2) that boundary vacancies prefer to collect into the high-density vacancy phases because of the additional relaxation, which parallel shifting of the grains affords, and (3) that the binding of vacancies to the boundary reduces the inter-granular spacing because this restores more bulk-like interatomic separations. These phenomena open the intriguing possibility that the application of tensile stress normal to grain boundaries in bcc metals generally drives transitions among these various structural phases, thereby providing new forms of boundary-vacancy interaction.

To explore this possibility, we consider the thermodynamic potential which is

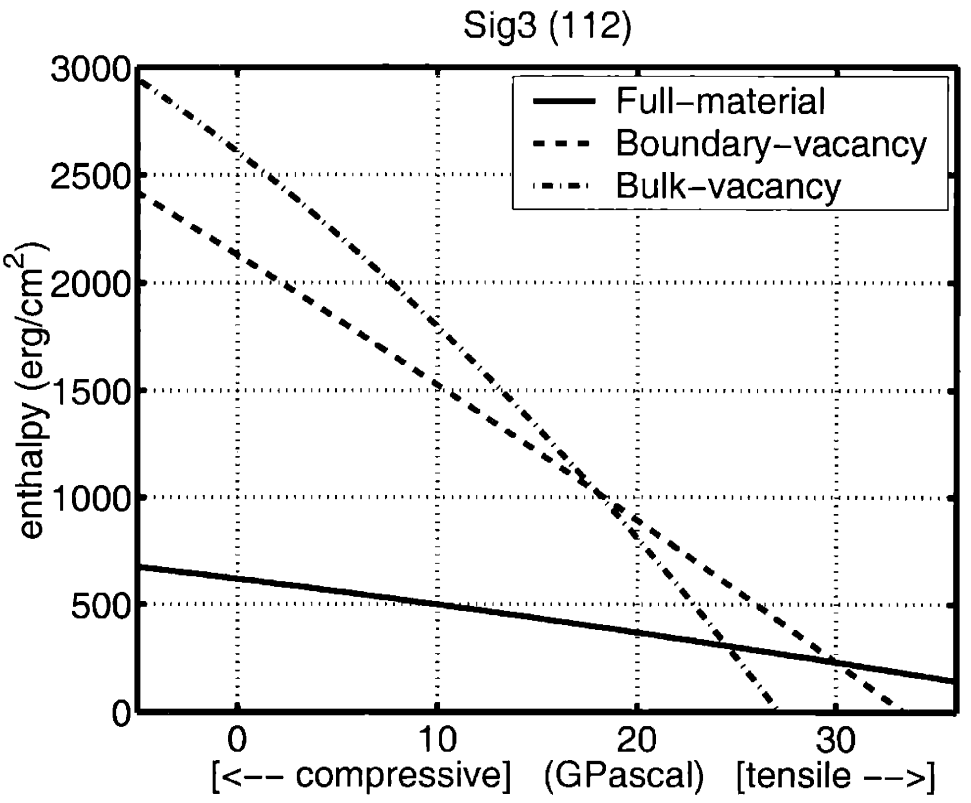

Figure 3-3: Enthalpies of $\Sigma 3(112)$ boundary as a function external stress for all three phases.

minimized under fixed external stress, the enthalpy. As a function of applied perpendicular stress σ, the enthalpy of a grain boundary structure relative to bulk is

$$\Delta\mathcal{H} = \Delta\mathcal{U}_o - \Delta x\,\sigma - \frac{1}{2}\Delta(1/k)\,\sigma^2 + \frac{1}{6}\Delta a\,\sigma^3 + \mathcal{O}(\sigma^4). \tag{3.2}$$

Here $\Delta\mathcal{U}_o$ is the difference in the ground-state energy per unit area, Δx is the difference in preferred perpendicular inter-granular separation, $\Delta(1/k)$ is the difference in compliance, and $\Delta a \equiv \Delta(\alpha/k^3)$ captures the difference in the non-quadratic behavior of the energies. Each of these parameters appears for each relevant phase in Tables 3.1-3.4.

As an example, Figure 3-3 shows the behavior of the enthalpy, relative to bulk, of the naturally occurring $\Sigma 3(112)$ boundary in its full-material, boundary-vacancy

Boundary	Binding energy per vacancy at high density [eV]	Binding energy per vacancy at low density [eV]
Σ3(112)	0.7	0.6
Σ3(111)	2.1	1.1
Σ9(114)	1.4	0.7
Σ9(221)	2.3	2.0
Σ11(113)	1.4	-7.1
Σ11(332)	1.4	-1.7

Table 3.5: Boundary-vacancy binding energies at high and low densities. (The Σ11 boundaries do not bind vacancies at low concentrations.)

and bulk-vacancy phases. Three first-order phase transitions (enthalpy crossings) are evident in the figure. At zero stress, as observed above, the full-material phase is the ground state of the boundary, and moreover, in the presence of vacancies, the vacancy phase has lower energy than the bulk-vacancy phase, indicating that vacancies prefer the boundary over the bulk. However, at an applied stress of about 18 GPa (σ_c^{emit}) within MGPT, the Σ3(112) boundary system undergoes a first-order phase transition in which the vacancy phase is no longer preferred, and the boundary ejects its vacancies into the surrounding bulk material. A second transition occurs near 25 GPa (σ_c^{bulk}), at which point the bulk-vacancy phase becomes lower in enthalpy than the full-material phase. This corresponds to the *spontaneous* formation of vacancies in bulk, indicating breakdown of the bulk material. The third transition occurs near 30 GPa (σ_c^{gb}). Were this transition accessible before the breakdown of the bulk material, it would correspond to spontaneous formation of boundary vacancies.

It is important to note that many modes of failure in addition to spontaneous formation of vacancies are accessible to the bulk and boundaries. The transition stresses which we report for breakdown, therefore, can be regarded only as upper-bounds when making comparisons to experimental results.

Table 3.6 presents the stresses for the above three transitions for all boundaries in our study. In all cases, the emission stress is accessible before breakdown of the

Boundary	σ_c^{emit} [GPa]	σ_c^{bulk} [GPa]	σ_c^{gb} [GPa]
$\Sigma 3(112)$	18	25	30
$\Sigma 3(111)$	15	20	66
$\Sigma 9(114)$	19	21	42
$\Sigma 9(221)$	38	24	10
$\Sigma 11(113)$	21	27	45
$\Sigma 11(332)$	31	27	22

Table 3.6: Critical stresses for the phase transitions discussed in the text: emission of vacancies from the boundary into the bulk (σ_c^{emit}), breakdown of the bulk through spontaneous formation of vacancies (σ_c^{bulk}), spontaneous formation of vacancies at the boundary (σ_c^{gb}).

Boundary	σ_c^{emit} [GPa]	σ_c^{bulk} [GPa]	σ_c^{gb} [GPa]
$\Sigma 3(112)$	17	25	29
$\Sigma 3(111)$	11	20	40
$\Sigma 9(114)$	9	21	61
$\Sigma 9(221)$	26	24	6
$\Sigma 11(113)$	56	27	81
$\Sigma 11(332)$	37	27	31

Table 3.7: Critical stresses for the same transitions as in Table 3.6, but at 3.3% vacancy concentration.

bulk material through spontaneous formation of vacancies. Moreover, except for the outlying behaviors of the $\Sigma 9(221)$ and $\Sigma 11(332)$ boundaries, vacancies always first form spontaneously in the bulk before they do so on the boundaries.

To verify that these results are not artifacts of the high-density vacancy phase, we repeat the above enthalpy analysis for boundaries with low densities of vacancies using the data of Table 3.4. As Table 3.7 summarizes, we again observe the same transitions. The $\Sigma 11$ boundaries do not bind vacancies at low concentrations (Table 3.5), and therefore, the transition stresses for the emission of vacancies for these boundaries are not physically relevant. For the lower Σ boundaries (except the $\Sigma 9(221)$ boundary, which again exhibits an outlying behavior), diluting the vacancy concentration reduces the critical emission stress at which the boundaries emit boundary vacancies into the bulk (σ_c^{emit}), thus making this transition more accessible.

Finally, as we expect from the fact that boundary vacancies are more stable in high concentrations, the stress required to induce formation of vacancies on the boundaries (σ_c^{gb}) at low densities is generally greater than for the high-density vacancy phase. As a last consistency check on our analysis, we note that the stress for breakdown of the bulk through the spontaneous formation of vacancies (σ_c^{bulk}), as a characteristic of the perfect crystal and not the boundary, remains essentially unchanged between the two independent sets of calculations for low and high boundary vacancy concentrations.

3.4 Conclusions

We expect that the following conclusions likely hold generally for the interactions among vacancies and tilt grain boundaries: (1) consistent with the traditional view of grain boundaries as diffusion pathways, vacancies prefer the boundaries over the bulk at low stresses, (2) boundary vacancies prefer to collect into high-density vacancy phases, (3) application of sufficient tensile stress to a boundary induces a structural phase transition which drives the vacancies from the boundaries into the bulk, thereby shutting off pipe diffusion along the boundary. The last of these conclusions in particular may have important implications for crack growth through pipe-diffusion assisted

void growth and void formation at grain boundaries.

Finally, in terms of precise *quantitative* predictions of the critical stresses characterizing these phenomena, it is important to bear in mind that the particular interatomic potential which we have employed (MGPT), although one of the most reliable for Mo, is known to exaggerate energy scales for complex structures[4]. We therefore expect to find these same transitions, but most likely at lower stresses, when studied either experimentally or *ab initio*.

Chapter 4

Ab initio study of grain boundaries in molybdenum

Abstract:

Our previous work, based upon atomistic potentials [3] indicated that multiple structural phases compete for the ground state of symmetric tilt grain boundaries in bcc materials and that external stress may drive vacancy-mediated transitions among these phases. In the present study, we verify these predictions through *ab initio* density-functional calculations on the naturally occurring twin $\Sigma 3(112)\ \langle 110 \rangle$. Specifically, we confirm that the application of external stress drives a structural phase transition for this boundary which causes it to emit vacancies into the surrounding bulk material.

4.1 Introduction

Understanding the nature of the brittleness of Molybdenum has been a challenge for researchers in the past three decades. While some experiments[57, 59] demonstrate that brittleness is an intrinsic property of Molybdenum unrelated to the presence of impurities with inter-granular fracture occuring at tensile stresses of 1.7 GPa, other experiments show the nature of spallation and the stress at which it occurs to depend on the material preparation.[33, 60]. These latter experiments show trans-granular spall at ~2.5 GPa for large grained samples[60] and an inter-granular spall at 15-25 GPa for fine-grained samples[33].

Our previous work explored the effects of impurities on the brittleness of Molybdenum by performing an atomistic trend study of Molybdenum grain boundaries. We studied the symmetric tilt grain boundaries around the ⟨110⟩ axis (as they dominate the recrystallization texture[58]), using the model generalized pseudopotential theory (MGPT) potential of Moriarty and coworkers[29, 30, 31, 32, 41], which has been shown to successfully predict various properties of Molybdenum, such as the cohesive, elastic, vibrational, thermal and melting properties[31] as well as the ideal shear strength and self-interstitial and vacancy formation energies[32].

After performing force and energy calculations of over 400,000 configurations within this potential, our results indicated that (a) consistent with the traditional view of grain boundaries as diffusion pathways, vacancies prefer the boundaries over the bulk at low stresses, (b) boundary vacancies prefer to collect into high-density vacancy phases along the boundaries, and (c) application of sufficient tensile stress to a boundary induces a structural phase transition which drives the vacancies from the boundaries into the bulk, thereby shutting off the boundary as a pipe diffusion pathway.

Although the MGPT is among the most reliable interatomic potentials for Mo, it is known to exaggerate energy scales for complex structures[4]. While our results with the MGPT placed the vacancy transition stresses at quite high values (15-38 GPa), spallation experiments indeed reach tensile stresses at least as high as 25 GPa [33],

	AI	Expt	Error
a	3.10	3.15	-1.6%
K	1.60	1.36	18%

Table 4.1: Mo lattice constant a (Å) and bulk modulus (Mbar). (Expt [54])

placing our prediction within the experimentally accessible range of stresses. Given the tendency of the MGPT to exaggerate energy scales, however, it is important to confirm our prediction and determine a reliable, *ab initio* value for the transition stress. As *ab initio* trend studies of large systems is computationally very demanding, we here focus on the most important and commonly occuring boundary, the naturally occurring $\Sigma 3(112)$ $\langle 110 \rangle$ twin.

4.2 Procedure

To minimize the computational demands of this study, we begin with MGPT relaxed structures as initial configurations for the *ab initio* calculations and relax these structures both electronically and ionically. These calculations are performed within the total-energy plane-wave density functional pseudopotential approach [14], using the Perdew-Zunger [61] parameterization of the Ceperley-Alder [2] exchange-correlation energy with Kleinman-Bylander [7] nonlocal pseudopotentials with s, p and d channels optimized according to the procedure of Rappe *et al.* [20]. With this potential, we find that plane wave basis sets with an energy cutoff of 45 Ryd serve to converge total energies to within 0.01 eV/atom. Table 4.1 summarizes the predictions of our pseudopotential at this plane wave cutoff for the bulk material, showing that our *ab initio* approach gives reasonable agreement with experiment for the lattice constant and bulk modulus.

Our MGPT study identified the ground state structural phases of the symmetric tilt grain boundaries around the $\langle 110 \rangle$ axis as either (a) the "full-material phase" in which grain boundaries have the same amount of material as the naïve coincident site lattice (CSL) construction, or (b) the "vacancy phase" in which one half-plane of

atoms from the layer adjacent to the boundary has been removed. (Chapter 3 gives detailed discussion of the considerations used in identifying these phases and their structural properties.) In this work, we use *ab initio* methods for the first time to explore the effects of external stress on these structures for the $\Sigma3(112)$ $\langle 110 \rangle$ twin boundary.

To model the boundary we employ a periodic supercell of repeating boundaries with alternate orientations separated by 12 layers of atoms so as to minimize the boundary-boundary interactions and with sufficient in-plane extent so that a single boundary vacancy in the supercell corresponds to the removal of one half-plane of atoms, for final supercell dimensions of a×b×c Å^3. To sample the Fermi surface with a total energy convergence of 0.01 eV/atom, we employ a non-zero electronic temperature of $k_BT = 0.1$ eV and sample the Brillouin zone of the supercell with 8 k-points, $k_1 = k_2 = \frac{1}{4}, k_3 \in \pm\{\frac{1}{16}, \frac{3}{16}, \frac{5}{16}, \frac{7}{16}\}$.

Finally, to study the effects of external stress, we apply a series of external strains, and perform full *ab initio* electronic and ionic relaxations at each strain. To provide reference data on vacancies, we performed the same sequence of calculations for a cell of the same size, containing a single vacancy embedded in otherwise a $\Sigma3(112)$ $\langle 110 \rangle$ commensurate perfect bulk material.

4.3 Results

Figure 4-1 shows the total interfacial energy for each boundary phase as a function of external strain along with a cubic polynomial fit to the data of the form

$$\mathcal{U} = \mathcal{U}_o + \frac{1}{2}k(x - \Delta x)^2 + \frac{1}{6}\alpha(x - \Delta x)^3 + \ldots \tag{4.1}$$

where $\mathcal{U}_o$ is the ground state energy of the structure, x is the expansion of the cell perpendicular to the boundary, k represents the quadratic response of the energy per unit area per boundary as the cell expands, α captures anharmonic behaviors, and Δx denotes expansion of the bulk material due to the presence of the boundary.

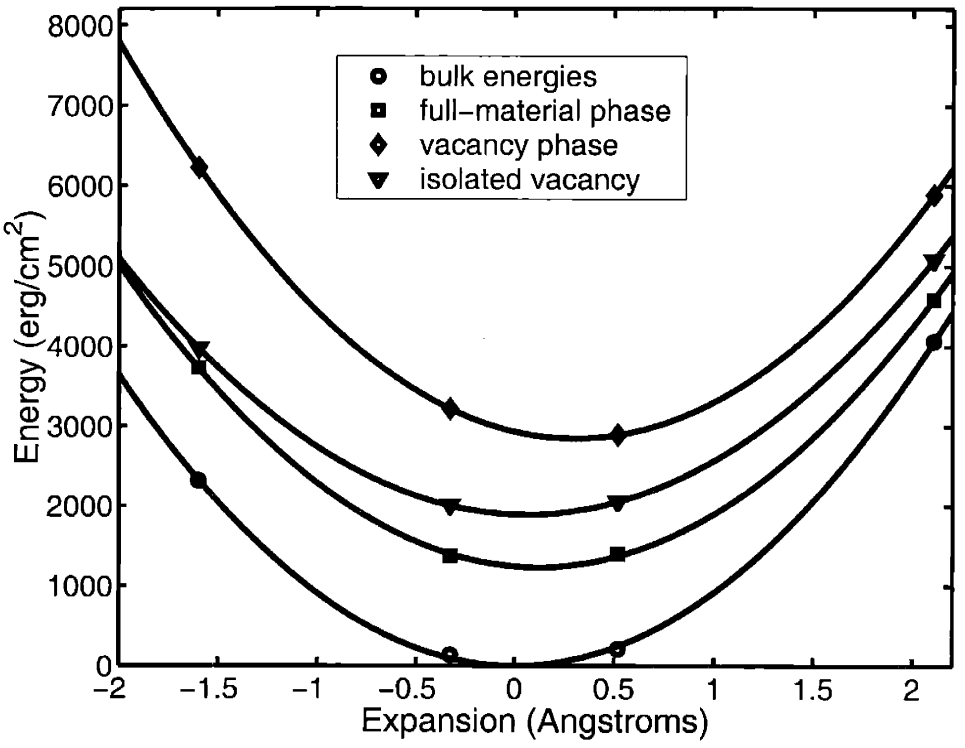

Figure 4-1: Energies of $\Sigma 3(112)$ boundary as a function of lattice expansion for all three phases.

Table 4.2 gives the $\mathcal{U}_o$, Δx, $\Delta(1/k)$, and $\Delta(a) \equiv \alpha/k^3$ values calculated for the full material and vacancy structural phases of $\Sigma 3(112)$ boundary as well as for an isolated vacancy. Consistent with our previous atomistic results reported in Chapter 3, the full-material phase is the lowest energy structure at zero stress with an interfacial energy very close to the predictions of the atomistic potential, 610 mJ/m^2, which were consistent with the experimental results[58]. This level of quantitative agreement in the energy of this boundary is not unexpected because the MGPT potential has been fit to reproduce the properties of bulk Molybdenum and, as such, is expected to predict well the energetics of bulk-like structures. Table 4.2 also confirms our previous MGPT result that at zero stress, the vacancy phase (1420 mJ/m^2) is much higher in energy than the full-material phase (620 mJ/m^2). Finally, the fact that the vacancy energy which we provide in the table is within 7% of the experimental value and MGPT prediction of 3 eV[32] indicates that the supercell in our calculations,

Phase	$\mathcal{U}_o$ [mJ/m^2]	Δx [Å]	$\Delta(1/k)$ [mJ/m^4] $\times 10^{-20}$	$\Delta(a)$ [m^7/mJ^2] $\times 10^{-28}$
Full-material	620	0.11	350	220
Vacancy	1420	0.30	120	170
Isolated vacancy	1890 (2.78eV)	0.06	220	290

Table 4.2: Energies ($\mathcal{U}_o$), perpendicular expansions (Δx), compliances ($\Delta(1/k)$) and anharmonic coefficients (Δa) relative to bulk for the structural phases of $\Sigma 3(112)$ boundary.

though relatively small is sufficiently large to provide reliable results for the isolated vacancy.

As discussed in our previous atomistic studies (Chapter 3), to transform physically into the full-material phase, the vacancy phase must first expel its vacancies into the surrounding bulk material. From Table 4.2, we see that, consistent with our previous atomistic results, this "bulk-vacancy" phase (full material phase boundary plus isolated vacancies in the bulk material) indeed has higher energy than the vacancy phase at zero external stress. We thus have the first *ab initio* verification of our previous result that at zero stress, vacancies prefer to be at the grain boundary instead of inside the bulk and that this boundary can serve as a pathway for pipe-diffusion. Section 4.4 explores further the implications of this result.

Whereas the energies of the grain-boundary phases suffice to predict behavior at zero stress, to understand the effects of an applied stress, we must consider the enthalpies of the various phases as the thermodynamic potential minimized under fixed external stress. Under the requisite Legendre transformation, (4.1) becomes

$$\Delta\mathcal{H} = \Delta\mathcal{U}_o - \Delta x\,\sigma - \frac{1}{2}\Delta(1/k)\,\sigma^2 + \frac{1}{6}\Delta a\,\sigma^3 + \mathcal{O}(\sigma^4), \tag{4.2}$$

where $\Delta\mathcal{U}_o$ is the difference in the ground-state energy per unit area, Δx is the difference in preferred perpendicular inter-granular separation, $\Delta(1/k)$ is the difference in compliance, and $\Delta a \equiv \Delta(\alpha/k^3)$ captures anharmonic behavior.

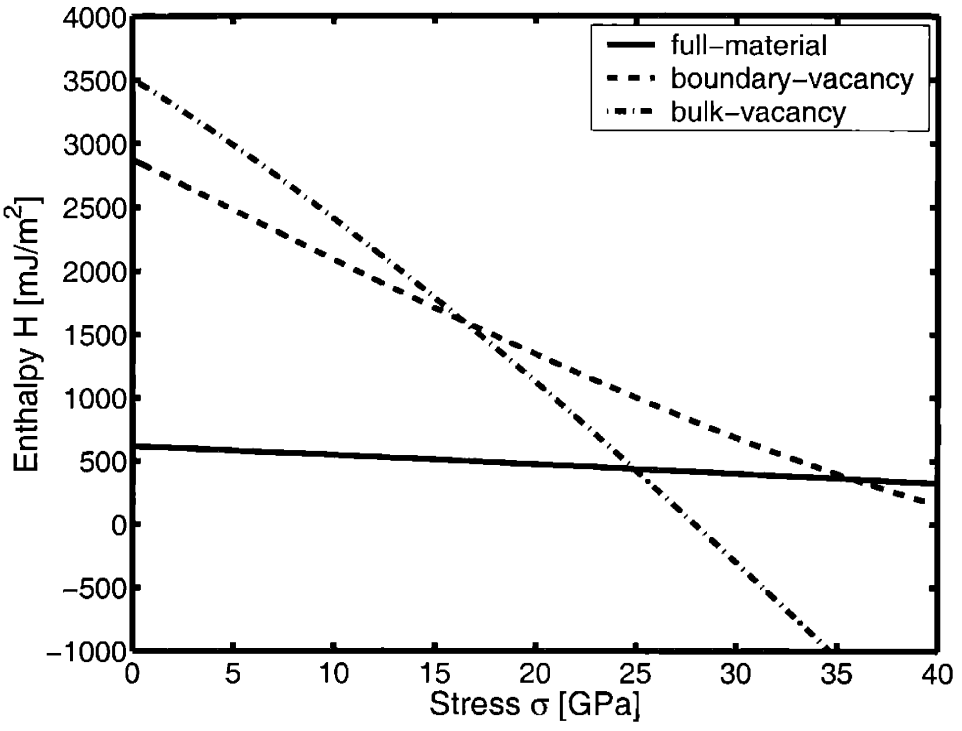

Figure 4-2: Enthalpies of $\Sigma 3(112)$ boundary as a function external stress for all three phases.

Figure 4-2 shows the enthalpy of each relevant phase as a function of external stress, evaluated according to (4.2) with the parameters which Table 4.2 provides. The figure shows the existence of three first-order phase transitions (enthalpy crossings). The figure shows, as discussed above, that at zero stress the full-material phase is the ground state of the boundary and that the boundary-vacancy phase has lower enthalpy than the bulk-vacancy phase (full-material phase with equal number of vacancies in the surrounding bulk material) so that if vacancies are present in the system, they prefer the boundary over the bulk. At an applied stress of about 16 GPa, however, the boundary-vacancy phase is no longer favored over the bulk-vacancy phase, the boundary ejects its vacancies into the surrounding bulk material and no longer serves as a pathway for pipe-diffusion. Near 24 GPa, a second enthalpy crossing occurs, which corresponds to spontaneous vacancy formation in bulk. A third transition, which occurs near 37 GPa, long after the breakdown of the bulk

material, indicates that if this transition were accessible, vacancies are last to form spontaneously on the boundary. This general framework of structural phase transitions is consistent with the MGPT findings. Moreover, the external stress required to eject the vacancies from the boundary into the surrounding bulk, and the stress at which spontaneous vacancies form inside the bulk are lower for the *ab initio* calculations than the MGPT calculations, whereas the breakdown of the boundary through spontaneous formation of vacancies is placed at a higher external stress.

When interpreting experiments in light of the above results, it is important to keep in mind that under stress, in reality, the material is likely to access many other modes of failure before the spontaneous formation of vacancies. The latter two enthalpy crossings, therefore, should be considered as upper-bounds to the breakdown of the material.

4.4 Conclusions

We have carried out the first *ab initio* study of vacancy mediated structural phase transitions in bcc molybdenum. We find that for the most common boundary, the naturally occurring $\Sigma 3(112)$ twin boundary, the full-material phase is the ground state structure at zero stress and that at tensile stresses less than 16 GPa, vacancies prefer the boundary over the bulk so that it may serve as a pathway to pipe-diffusion. However, application of a tensile stress in excess of 16 GPa drives a first-order structural phase transition which ejects the vacancies into the surrounding bulk and shuts down the boundary as a pipe-diffusion pathway.

The results of this *ab initio* study confirm several of the conclusions from our previous work employing atomistic potentials, in particular the existence of multiple competitive structural phases for the boundaries and a vacancy-ejection transition under application of large, but experimentally accessible tensile stress. However, due to cell-size limitations our *ab initio* calculations to date have explored only the dense-vacancy phase and not the dilute-vacancy phase. Thus, further *ab initio* studies will be needed to fully confirm our previous finding that vacancies not only prefer the

boundary over the bulk but that they also prefer to bind together into high-density clusters along the boundaries. However, the overall reliability of our MGPT findings to date strongly suggest that these other findings of our atomistic work likely will continue to hold true under further *ab initio* scrutiny.

Chapter 5

Atomistic and *ab initio* study of non-Arrhenius diffusion of Co adatoms on the magnetic Co(0001) surface

Abstract:

We present a multiscale theoretical study of the motion of a cobalt adatom on a Co(0001) surface. We begin with an atomistic molecular dynamics study and observe a transition from thermally activated diffusion to ballistic behavior at a temperature where recent experiments show an abrupt change in the character of surface evolution in ion erosion experiments [42]. Using transition state theory, we show that this transition corresponds to a low activation barrier for the adatom as it moves between the energetically favorable sites on the surface. In order to understand the physics underlying this behavior, we study the transition path using *ab initio* methods, which confirm our atomistic finding and demonstrate a close link between the motion of the adatom and the spin configuration of the material.

5.1 Introduction

The technological potential for high-density magnetic storage devices based upon the manipulation of electron spins, so-called spintronics[43], has brought recent attention to the physics of the growth and sputtering of elemental magnetic material surfaces such as that of cobalt. Recent experiments and modeling work [42] show that morphology of the Co(0001) surface under low energy ion erosion goes under an abrupt transition near 570 K from smooth layer-by-layer behavior to mounding at pitting, with the motion of adatoms playing a key role.

The present work represents a multilevel theoretical study of the underlying physics of motion of adatoms on the Co(0001) surface. We begin with a classical molecular dynamics study which shows, intriguingly, a transition in the nature of adatom diffusion from thermally activated diffusion to ballistic behavior somewhere near a temperature of 500 K. As this result comes from an atomistic, and thus a necessarily very approximate potential, to assure ourselves of its meaningfulness, we identify its underlying cause through the use of transition state theory (TST). We find this behavior in the atomistic model to result from a quite low activation barrier of 0.057 eV ($\approx k_B 660$ K) for diffusion of the adatom from fcc to hcp surface sites. In Section 5.4 we explore the transition pathway with *ab initio* methods, confirming this result and discovering that the motion of the adatom connects intimately with the electronic spins of the underlying material.

5.2 Classical Molecular Dynamics Calculation

By their very nature of attempting to approximate a complex many-body potential with a simple analytic form fitted to a limited amount of information, classical interatomic potentials are necessarily approximate. Often in fact, the variations in the predictions for any given process among different potentials are as large as the discrepancies between the predictions and experimental observations. Thus, knowing that we always intend to pursue any final conclusions with *ab initio* density-functional calcu-

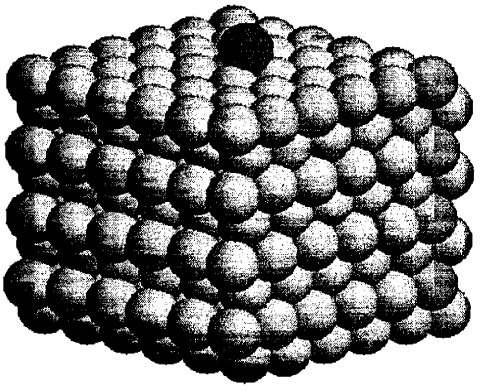

Figure 5-1: Periodic supercell used in molecular dynamics calculations: bulk cobalt atoms (light), adatom (dark).

lations, we adopt the philosophy of choosing a potential based upon (a) its providing agreement with a reasonable range experimental information *and* (b) its simplicity and relative ease of implementation.

In the above regard, we find the potential described by Levanov and co-workers[15] to suit our purpose well. This potential is formulated in the second moment tight-binding approximation (TB-ASA) of [45, 25], with a repulsive Born-Mayer term in the form of a pairwise sum of exponentially decaying interactions and an attractive band-structure term in the form of a sum of non-linear functions of a pairwise sum of exponentially decaying contributions. Specifically, we use the potential described in Reference [15], which generalizes somewhat the form of [45, 25] and provides parameters relevant to the treatment of cobalt. This potential reproduces the experimental values lattice constant and cohesive energy per atom of cobalt to within 0.008 Åand 0.009 eV, respectively, the various elastic moduli to within 0.22 Mbar (the bulk modulus is 1.99 Mbar) and reproduces *ab initio* calculations of the energy of cobalt clusters

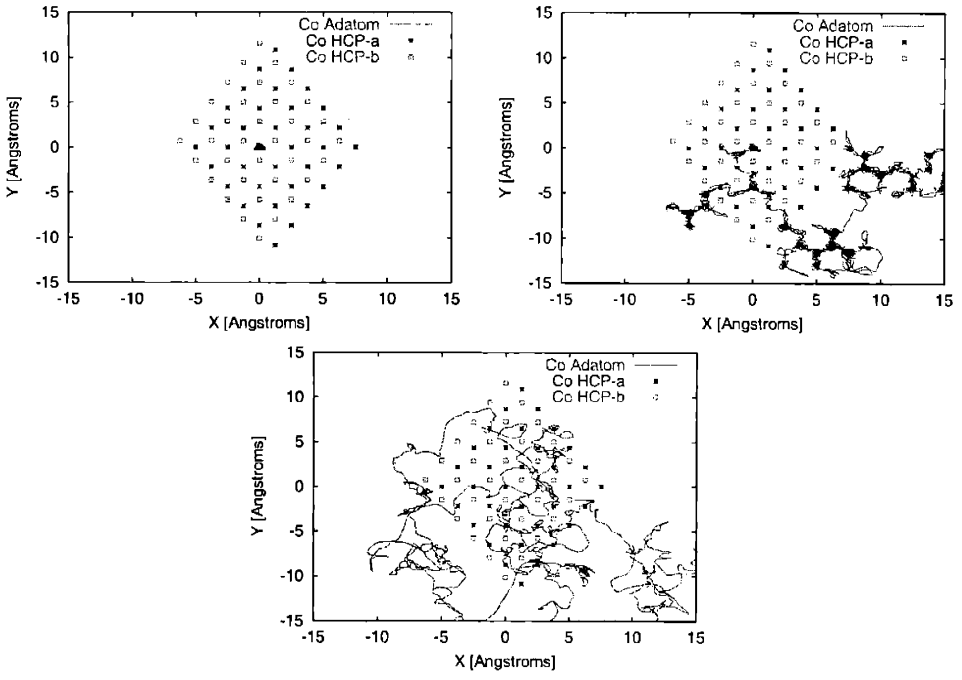

Figure 5-2: Molecular dynamics trajectory of adatom on Co(0001) surface: atomic sites of surface layer (squares), second layer (asterisks), adatom trajectory (lines), for T=100 K (a), T=300 K (b), T=800 K (c).

of 2-4 adatoms on the Cu(100) surface to within 0.09 eV. The latter finding is particularly encouraging because it indicates an ability to reproduce not only bulk but cluster and adatom properties. We also find the functional form simple and easy to implement with its pairwise interactions with a natural exponential cutoff.

To study the diffusion of Co adatoms on Co, we model the surface within the supercell approach using a slab geometry with periodic boundary conditions. The supercell for our calculations is 18.3 Å(8 layers) thick in the [0001] direction with $\langle 1000 \rangle$ triangular lattice vectors in the surface plane of length 12.5 Å. With the adatom included, this supercell contains a total of 289 atoms. (See Figure 5-1.) Using this geometry, we carry out classical molecular dynamics calculations allowing all atoms to evolve within the microcanonical ensemble using the Verlet algorithm with a time step of 2 fs ($\approx$ 1/20 of the zone-edge phonon period).

Figures 5-2a-c show the resulting trajectories for the adatom at temperatures of

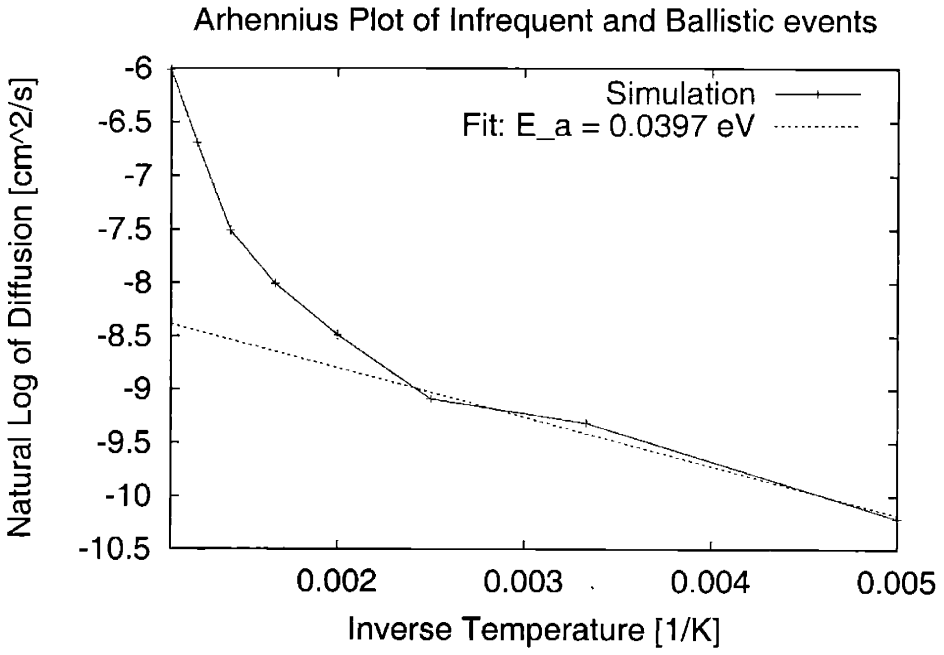

Figure 5-3: Arrhenius plot of diffusion vs inverse temperature with diffusive regime transition at $T \sim 400 - 500K$

100 K, 300 K and 800 K for runs of 0.3 ns. The trajectory at 100 K shows simply oscillation of the adatom about its initial site immediately above the second surface layer, a so-called *hcp site* where atoms in an hcp layer would reside. At 300 K, sufficient thermal energy is available for the adatom to begin to diffuse while clearly dwelling at either hcp sites (above the asterisks) or *fcc sites* (centered between three hcp sites), where atoms in an fcc layer would reside. At 800 K the trajectory of the adatom no longer dwells at particular locations and appears to meander randomly about the surface.

To quantify this behavior, we have computed autocorrelation functions for the adatom from our runs at each temperature T and extracted diffusion constants D according to

$$D = \lim_{t \to \infty} \frac{\langle |\vec{x}(t+t') - \vec{x}(t')|^2 \rangle_{t'}}{t}. \tag{5.1}$$

Figure 5-3 summarizes our results on an Arrhenius plot. Rather then exhibiting

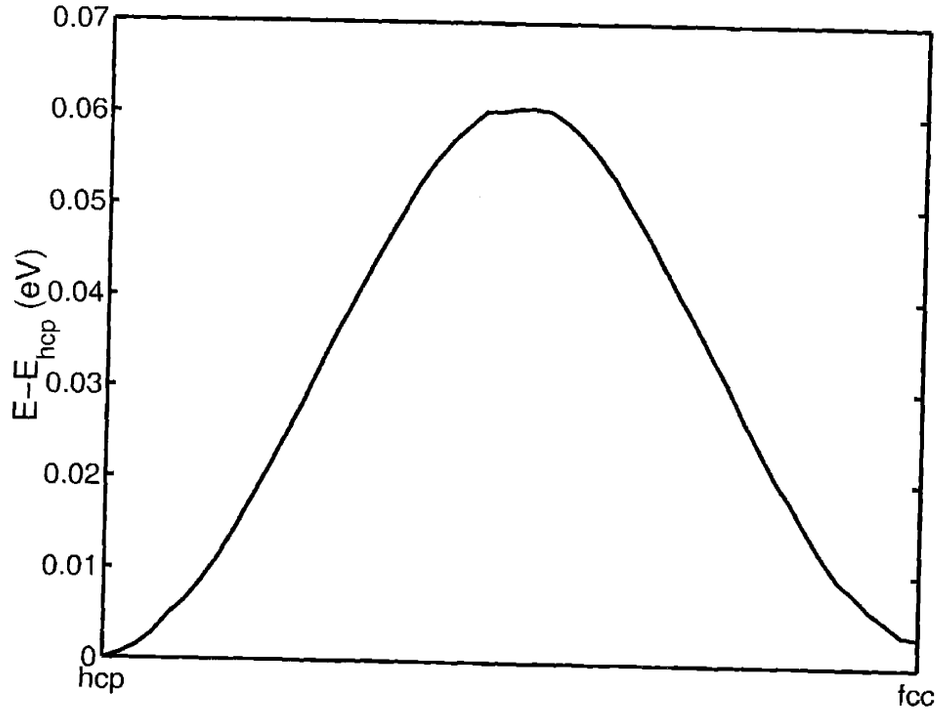

Figure 5-4: Energy along reaction coordinate connecting hcp and fcc sites from supercell used in molecular dynamics calculations.

the linear behavior characteristic of thermally activated processes, the results show noticeable curvature at temperatures around ~500 K, suggestively close to where experiments indicate a qualitative change in the evolution of surface morphology[42]. These results also suggest that kinetic Monte Carlo analyses based upon simple thermally activated diffusion cannot be relied upon to account properly for adatom diffusion beyond this temperature.

5.3 Transition State Analysis

To explore the physical mechanism underlying the departure from Arrhenius behavior in Figure 5-3, we consider the diffusion process in detail. The molecular dynamics trajectories in Figure 5-2 evolve by exploring alternating fcc and hcp sites. We therefore concentrate on these sites and the transition path between them.

From the relatively straight paths connecting the hcp and fcc sites in the molec-

ular dynamics trajectories, we identify the projection along the straight-line path in the 3N dimensional phase space connecting fully relaxed neighboring fcc and hcp configurations (with any arbitrary center of mass shift removed) as an appropriate generalized coordinate to characterize the transition. To calculate the optimal transition path, we step along this reaction coordinate and relax the structure with the value of the reaction coordinate as the only constraint.

Figure 5-4 summarizes the transition path results for both supercells. Note that the transition barrier for the molecular dynamics supercell is only 0.057 eV ($\approx k_B 660$ K). We should expect that as we approach this temperature, transitions over the barrier are no longer limited by the thermal fluctuations, and the usual Arrhenius behavior breaks down. We therefore trace the qualitative change in adatom diffusion in the molecular dynamics calculations at temperatures near 500 K directly to this very low transition barrier.

5.4 *Ab initio* Calculations

5.4.1 Procedure

A well known pitfall of empirical potentials is that they provide poor energies, particularly for configurations which do not resemble those to which the model has been fit. In this case, the potential was fit to the bulk elastic moduli and a few cobalt clusters adsorbed onto a *copper* surface, none of which necessarily reflect an adatom of cobalt changing coordination as it diffuses on a *cobalt* surface. Moreover, as [55] demonstrates for grain-boundaries in iron, atomistic potentials which do not treat explicitly the physics of electron spin often miss important exchange effects at interfaces. Thus, *ab initio* calculations are critical in confirming our finding of non-Arrhenius diffusion at around 500 K.

In order to study possible magnetic ordering effects, which require the exploration of multiple electronic ground states, with computationally demanding *ab initio* calculations, we must limit the size of our supercell. For our first principles electronic

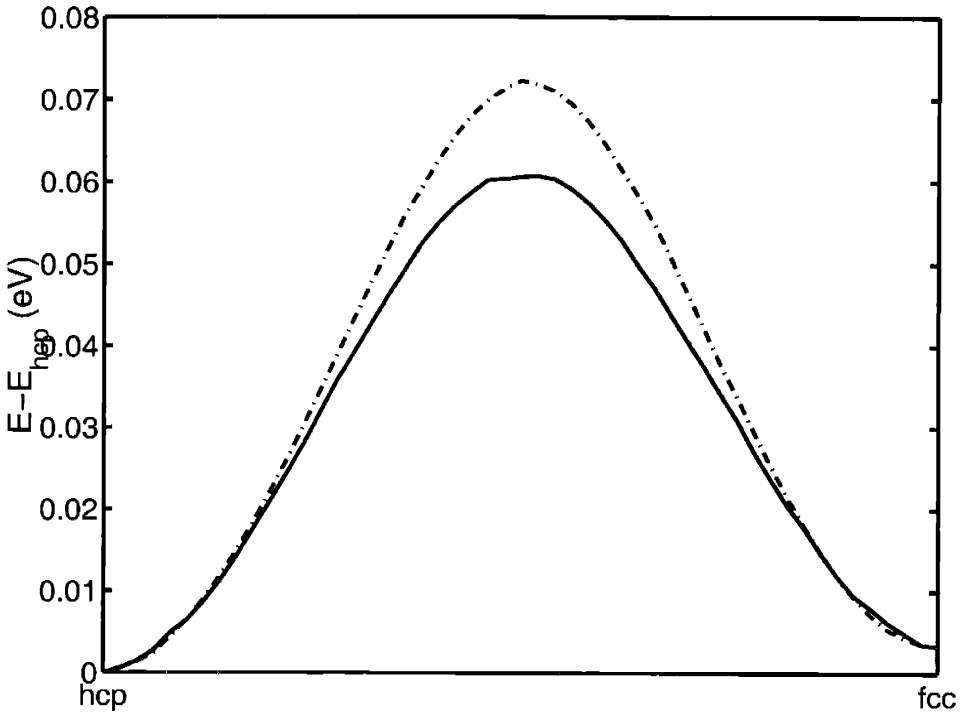

Figure 5-5: Energy along reaction coordinate connecting hcp and fcc sites: results from supercell used in molecular dynamics calculations (solid curve, 289 atoms), and from supercell used in *ab initio* calculations (dashed curve, 33 atoms).

structure calculations, we therefore employ a surface slab geometry with 8 layers in the [0001] direction but with 1/3 of the original linear dimension in the two surface directions. We believe the resulting supercell, 33 atoms including the adatom, to be acceptable because each adatom shares no neighbors with any of its images.

To confirm the appropriateness of such a small cell and to give a quantitative estimate of the corrections to any image effects, Figure5-5 compares the atomistic potential results for the transition barrier in the supercell of our *ab initio* calculations with our previous results within the much larger cell of Figure 5-4. The results in the figure show the pathway in the smaller cell to exhibit the same overall behavior with a transition barrier of 0.069 eV, only 0.012 eV more than the larger cell value. We therefore expect our *ab initio* results from the smaller cell to reflect the basic underlying physics but with a barrier slightly exaggerated by approximately 0.012 eV.

Our *ab initio* calculations employ the total-energy plane-wave density functional

	AI	Expt	Error
a (Å)	2.536	2.507	1.2%
c (Å)	4.163	4.070	2.3%
K (GPa)	180	160	-11.1%

Table 5.1: Cobalt lattice constants (a and c) and bulk modulus (K) as calculated *ab initio* in the present work (AI), measured in experiment (Expt), and the corresponding fractional error.

pseudopotential approach [14], describing electronic correlations using the Perdew-Zunger [61] parameterization of the Ceperley-Alder [2] exchange-correlation energy for the homogeneous electron gas and describing valence-core electron effects with Kleinman-Bylander nonlocal pseudopotentials with p and d channels[7] optimized according to the procedure of Rappe *et al.* [20]. With this potential, expanding the electronic wave functions in a basis of plane waves with kinetic energies up to 40 Ryd converges total energies to within 0.03 eV/atom. Table 5.1 summarizes the predictions of our pseudopotential at this plane wave cutoff for the bulk material, showing that our *ab initio* approach gives, without any adjustable parameters, quite reasonable agreement with experiment for the lattice constants and bulk modulus of Cobalt.

Our calculations of adatoms on the surface employ the thirty-three atom, eight layer supercell described above, with lattice constants in the two surface-plane directions set according to the *ab initio* values in Table 5.1. (The physics of system sets the lattice constant in the surface normal direction.) To perform Fermi surface integrations to within 0.05 eV/atom, we employ a non-zero electronic temperature of $k_BT = 0.2$ eV and sample the Brillouin zone of the supercell with 4 k-points, $k_1 = k_2 = \in \pm\frac{1}{4}$, $k_3 = 0$, where directions 1 and 2 are in the surface plane and direction 3 is the surface normal. Finally, for the atomic positions, all calculations below use as input the atomic configurations from the interatomic potential for the identical geometry, scaled according to the small difference in bulk lattice constants between the two models.

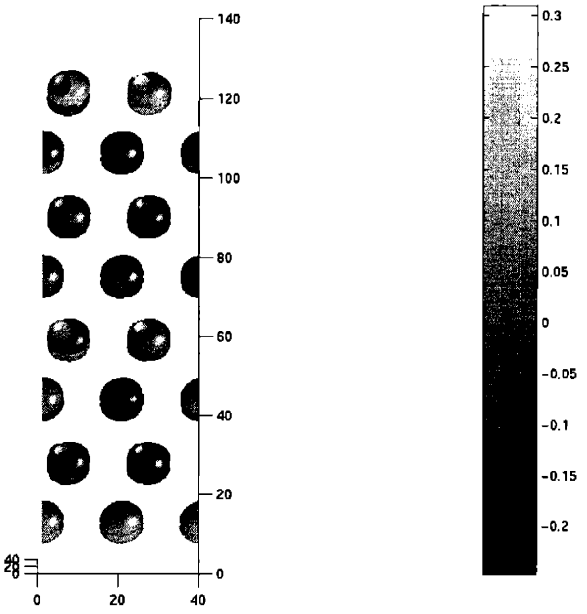

Figure 5-6: Spin density for the slab configuration with no adatom.

5.4.2 Results

The previous experience of others[9] and ourselves [55] with the electronic structure of interfaces in elemental magnetic materials (grain boundaries in iron in particular) show that such surfaces are prone to induce spatial oscillations in the electron spin density due to Fermi-surface ringing effects resulting from differing integration cutoffs at the Fermi surfaces for the up and down electron species. As the termination of a surface into vacuum is a far more severe disturbance to the electronic system than the tilt grain boundaries studied previously[9], we anticipate the effect to be quite strong for the current system. Thus, we first establish the spin configuration of the pure surface before proceeding to study the effects of adding adatoms.

Figure 5-6 shows the electronic spin density of the slab when relaxed from an arbitrary electronic configuration. The resulting electronic structure shows the expected spin ringing effect, but to an extent far greater than we observed previous at grain boundaries in iron[55], so strong in fact as to disrupt the ferromagnetic ordering of the bulk material.

To convince ourselves that such a configuration is characteristic of the ground-

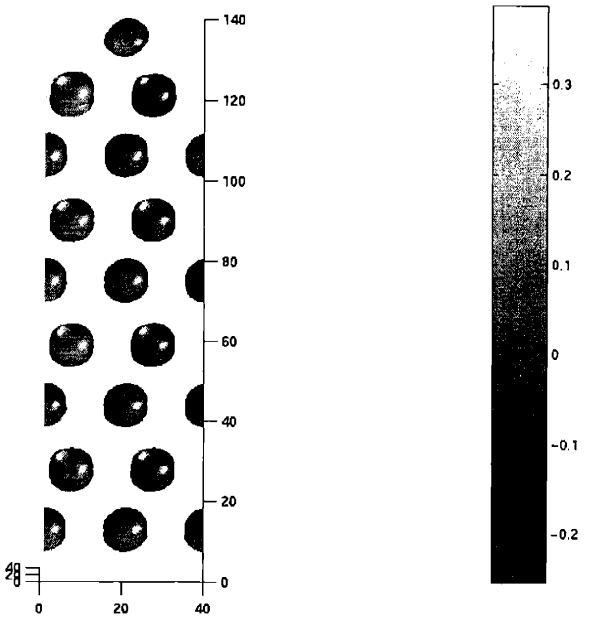

Figure 5-7: Spin density for the fully relaxed hcp adatom configuration.

state of the slab and not merely a local minimum into which the energy-functional minimization has become trapped, we have performed a large number of computational experiments on the surface slab, both with and without adatoms. We have performed electronic relaxations while fixing the occupancy of up and down electrons to reflect full spin-up polarization of all cobalt atoms ($4s^2 3d_\uparrow^5 3d_\downarrow^2$). Even under the constraint of three excess up electrons per cobalt atom, the electronic relaxation always results in some cobalt atoms with clear net down spin. We have also taken the electronic configurations corresponding to alternating spin orientations and forced the spins to align by fixing the self-consistent potential to what it would be were the spins to all have been aligned and even exaggerating the effect,

$$\begin{aligned} V'_\uparrow(r) &= \frac{V_\uparrow(r)+V_\downarrow(r)}{2} - (1+\alpha)\,|V_\uparrow(r)-V_\downarrow(r)| \\ V'_\downarrow(r) &= \frac{V_\uparrow(r)+V_\downarrow(r)}{2} + (1+\alpha)\,|V_\uparrow(r)-V_\downarrow(r)|\,, \end{aligned}$$

where $\alpha > 0$ is the fractional enhancement. Even with simple flipping of the potential ($\alpha = 0$), we find the alternation in the net spin orientation to remain unaffected.

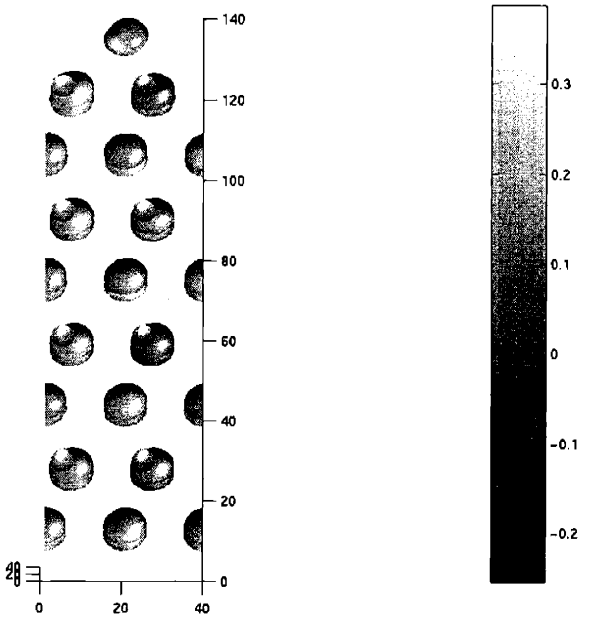

Figure 5-8: Spin density for the hcp configuration, obtained from flipping the potential so as to flip the densities.

Values of $\alpha \approx 0.5$ do result in complete ferromagnetic alignment; however, in all cases, we always find the configurations with forced alignment to have very high energies and always to relax back to configurations with the original misaligned configurations.

As an illustrative example, taking the fully relaxed hcp adatom configuration of Figure 5-7 and forcing its spins to align to produce the configuration in Figure 5-8 increased the total energy of the system by 700 eV/atom, two orders of magnitude larger than the binding energy of the solid. Upon relaxation, despite the extremely excited nature of this electronic state, the system converged directly back to the initial configuration in Figure 5-7. As a second example, we took this quite stable configuration and removed the adatom to produce the surface configuration of Figure 5-6. We then subjected this slab to spin alignment, which again radically increased the system energy. Upon electronic relaxation, the system again recovering the initial mixed spin configuration.

From the above considerations, we conclude that, despite the ferromagnetic nature of the bulk material, the intrinsic electronic structure of the Co(0001) surface, with or

without adatoms, indeed involves misaligned spins and that these spin configurations are quite stable. Figure 5-6 represents the lowest energy configuration we have yet to find for the surface configuration and so we shall take it as characteristic of the configuration of the surface.

Having established the nature of the electronic structure of the surface, we now consider the addition of an adatom. Figure 5-7 shows the most stable electronic configuration which we have found for an atom at an hcp site. The adatom aligns with the majority spin carrier of the bulk, while the atoms in the slab directly underneath the adatom have electron spin in the opposite direction.

To understand the interaction of the motion of the adatom with the underlying electronic structure, we now recalculate the electronic structure as the adatom moves from the initially relaxed hcp configuration of Figure 5-7 through the transition state identified from the atomistic calculations in Section 5.3 to the fcc site. To reflect the electronic system's adiabatic following of the ionic motion within the Born-Oppenheimer separation, we first take the electronic wave functions from Figure 5-7 and relax them in the presence of the ionic arrangement of the transition state, and we then take the resulting wave functions and relax them within the ionic arrangement of the fcc configuration.

Figure 5-9 compares the three resulting electronic configurations with the first panel repeating the information from Figure 5-7. From this figure, we see that the spin of the adatom increases strongly as it moves from the hcp site to the transition state (top right panel) and that, intriguingly, in moving to the stable fcc site (bottom panel), the adatom flips its spin. We therefore find the spin arrangement of the electrons and the motion of the adatom to be intimately interconnected with the adatom spin flipping as it goes over the transition barrier between hcp and fcc sites.

We now return to the transition state analysis of the configurations in Figure 5-9. Figure 5-10 compares the transition state path obtained from the atomistic molecular dynamics calculations with the *ab initio* result. The *ab initio* transition path shows the same overall behavior as the atomistic curve, and places the barrier energy at a lower value than the classical barrier, at 0.036 eV ($\approx k_B 420$ K), in close alignment

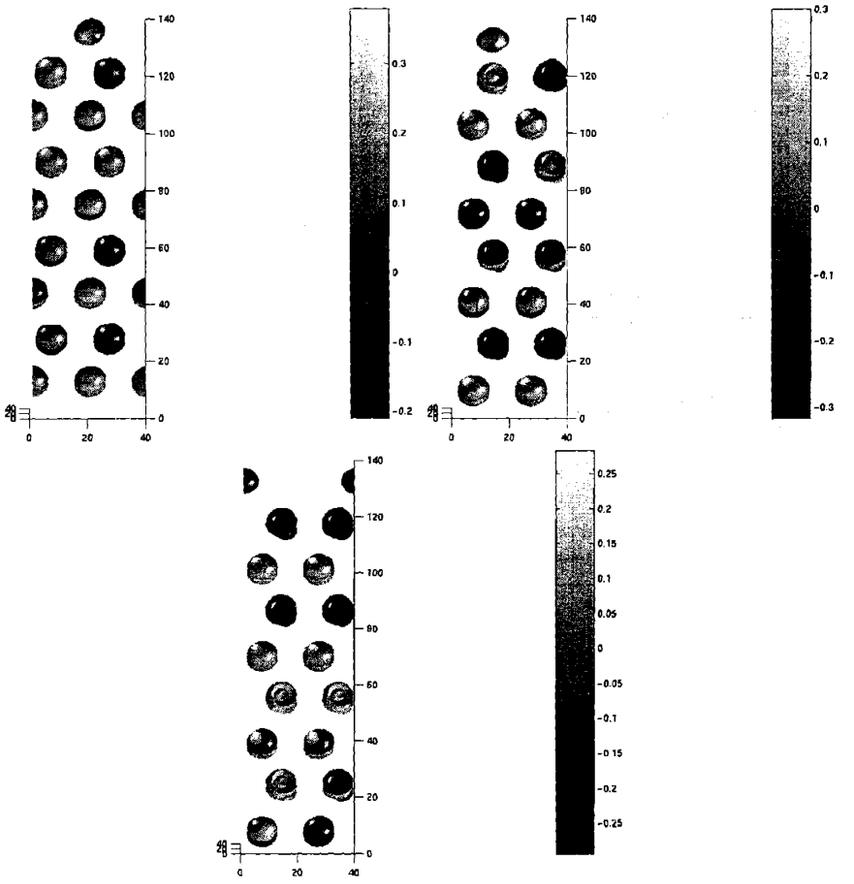

Figure 5-9: Spin densities for the hcp, intermediate and fcc configurations.

with the experimental observations.

5.5 Conclusions

We have performed both classical molecular dynamics and *ab initio* calculations to understand the changes in the nature of cobalt adatom motion from thermally activated diffusion to ballistic behavior as it moves on Co (0001) surface. We observed from our classical transition state theory studies that this change in behavior of the adatom is a result of the low barrier energy on the surface. To confirm this result, we then investigated this transition path using *ab initio* methods. Our results show that (a) despite the ferromagnetic nature of bulk cobalt, the stable electronic configuration

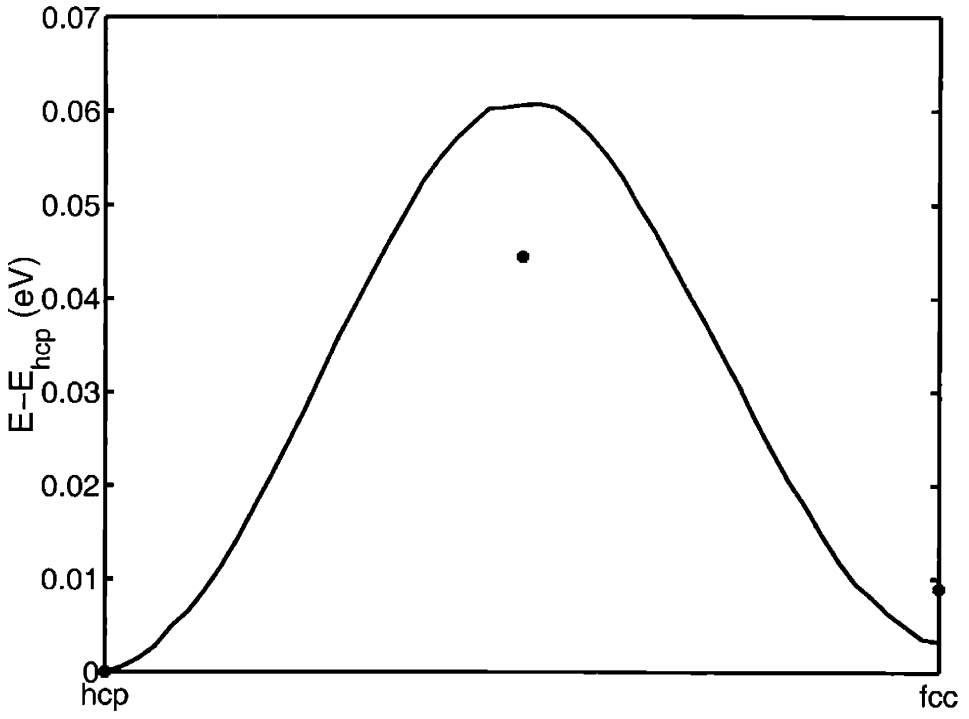

Figure 5-10: Energy along reaction coordinate connecting hcp and fcc sites: results from interatomic potential (dashed curve) and from *ab initio* calculations within the the same cell (stars, 33 atoms).

of the Co (0001) surface involves misaligned spins, (b) as the adatom moves between the energetically favorable hcp and fcc sites on the surface, it flips its spin, and (c) the barrier energy for this transition path including the spin flip of the adatom is in good agreement with the experiments.

The results of this *ab initio* study confirm the conclusions from the classical molecular dynamics study and identify the existence of a low surface barrier energy as possibly the physics underlying the change in the nature of surface evolution observed in experiments. Finally, our *ab initio* results suggest that this low energy barrier is closely linked to the spin configuration of the slab in conjunction with that of the adatom as it moves along the transition path. This intriguing link between the surfaces microscopic magnetic structure and macroscopic morphological evolution would be impossible to identify without our application of *ab initio* techniques.

Bibliography

[1] W. Xu J.B. Adams. *Surf. Sci.*, 301:371, 1994.

[2] D.M. Ceperley B.J. Alder. *Physical Review Letters*, 45:566, 1980.

[3] D. Yesilleten T.A. Arias. *Physical Review B*, 64:174101, 2001.

[4] S. Ismail-Beigi T.A. Arias. *Physical Review Letters*, 84:1499, 2000.

[5] A.P. Sutton R.W. Balluffi. *Interfaces in Crystalline Materials.* Clarendon, Oxford, 1995.

[6] R.W. Balluffi. *Phys. Stat. Sol.*, 31:443, 1969.

[7] L. Kleinmann D.M. Bylander. *Physical Review Letters*, 48:1425, 1982.

[8] A.E. Carlsson. *Physical Review B*, 44:6590, 1991.

[9] K. Hampel D.D. Vvedensky S. Crampin. *Physical Review B*, 47:4810, 1993.

[10] K. M. Miller K. W. Ingle A. G. Crocker. *Acta. Meta.*, 29:1599, 1981.

[11] K. W. Ingle A. G. Crocker. *J. Nuclear Materials*, 69-70:667, 1978.

[12] K. W. Ingle A. G. Crocker. *Phil. Mag.*, 37:297, 1978.

[13] Y. Itsumi D.E. Ellis. *J. Mat. Res.*, 11:2214, 1996.

[14] M.C. Payne et al. *Rev. Mod. Phys.*, 64:1045, 1992.

[15] N.A. Levanov et. al. *Physical Review B*, 61:2230, 2000.

[16] S.M. Foiles. *Physical Review B*, 48:4287, 1993.

[17] R.W. Balluffi A.V. Granato. *Dislocations in Solids*, 4:1, 1979.

[18] H. Hasegawa. *J. Phys. Soc. Jpn.*, 49:178, 1980.

[19] J. Hubbard. *Physical Review B*, 19:2626, 1979.

[20] A. Rappe K. Rabe E. Kaxiras J.D. Joannopoulos. *Physical Review B*, 41:2127, 1990.

[21] P. Hohenberg W. Kohn. *Physical Review B*, 136:864, 1964.

[22] J.C. Slater G.F. Koster. *Physical Review B*, 39:1498, 1954.

[23] G.L. Krasko. *Physical Review B*, 36:8565, 1987.

[24] G.L. Krasko. *Defect - Interface Interactions Symposium, Boston MA, Mater. Res. Soc; Pittsburgh, PA*, page 369, 1993.

[25] V. Rosato B. Guillope B. Legrand. *Philos. Mag. A*, 59:321, 1989.

[26] J.P. Hirth J. Lothe. *Theory of Dislocations.* Wiley, New York, second edition, 1982.

[27] M.Aoki. *Physical Review Letters*, 71:3842, 1993.

[28] R. Watanabe A. Nogami T. Matsumiya. *Materials Science Forum*, 204-206:337, 1996.

[29] J.A. Moriarty. *Physical Review B*, 38:3199, 1988.

[30] J.A. Moriarty. *Physical Review B*, 42:1609, 1990.

[31] J.A. Moriarty. *Physical Review B*, 49:12431, 1994.

[32] W. Xu J.A. Moriarty. *Physical Review B*, 54:6941, 1996.

[33] L.E. Murr. *J. Appl. Phys.*, 47:1364, 1976.

[34] G.L. Krasko G.B. Olson. *Physical Review B*, 40:1153, 1989.

[35] R. Wu A.J. Freeman G.B. Olson. *Physical Review B*, 53:7504, 1995.

[36] S. Tang A.J. Freeman G.B. Olson. *Physical Review B*, 50:1, 1994.

[37] H.J. Monkhorst J.D. Pack. *Physical Review B*, 13:5188, 1976.

[38] D. Pettifor. *Bonding and Structure of Molecules and Solids.* Claredon Press, Oxford, 1995.

[39] D.G. Pettifor. *Physical Review Letters*, 63:2480, 1989.

[40] H. Hasegawa D.G. Pettifor. *Physical Review Letters*, 50:130, 1983.

[41] J.A. Moriarty R. Phillips. *Physical Review Letters*, 66:3036, 1991.

[42] O. Malis J.D. Brock R.L. Headrick M. Yi J.M. Pomeroy. *Physical Review B*, 66:035408, 2002.

[43] X. Waintal E.B. Myers P.W. Brouwer D.C. Ralph. *Physical Review B*, 62:12317, 2000.

[44] D. Farkas P. L. Rodriguez. *Scripta metall.*, 30:921, 1994.

[45] F. Cleri V. Rosato. *Physical Review B*, 48:22, 1993.

[46] S. Sawada. *Vacuum*, 41:612, 1990.

[47] W. Kohn L.J. Sham. *Physical Review A*, 140:1133, 1965.

[48] M.W. Finnis J.E. Sinclair. *Phil. Mag. A*, 50-53:45161, 1984.

[49] E. C. Stoner. *Proc. R. Soc. London, Ser.*, page 339, 1939.

[50] M.P. Allen D.J. Tildesley. *Computer Simulation of Liquids.* Oxford University Press, Oxford, 1987.

[51] W. Zhong G. Overney D. Tomanek. *Physical Review B*, 47:95, 1993.

[52] L.H. Van Vlack. *Trans. Amer. Inst. Min. Met. End.*, 191:251, 1951.

[53] J.R. Wilson. *Met. Rev.*, 10:381, 1965.

[54] C. Woodard S. Kajihara L.H. Yang. *Physical Review B*, 57:13459, 1998.

[55] D. Yesilleten M. Nastar T.A. Arias T. Paxton S. Yip. *Physical Review Letters*, 81:2998, 1998.

[56] K. S. Cheung S. Yip. *Modell. Simul. Mater. Sci. Eng.*, 2:865, 1994.

[57] H. Kurishita A. Oishi H. Kubo H. Yoshinaga. *J. Jpn. Inst. Met.*, 47:539, 1983.

[58] S. Tsurekawa T. Tanaka H. Yoshinaga. *Materials Science and Engineering*, page 341, 1994.

[59] T. Tanaka S. Tsurekawa H. Nakashima H. Yoshinaga. *J. Jpn. Inst. Met.*, 58:382, 1994.

[60] V.K. Golubev S.A. Novikov Y.S. Sobolev N.A. Yukina. *Strength of Materials*, 17:515, 1985.

[61] J. Perdew A. Zunger. *Physical Review B*, 23:5048, 1981.